Vortex shedding effects in grid-generated turbulence

G. Melina,* P. J. K. Bruce, and J. C. Vassilicos
Department of Aeronautics, Imperial College London, London SW7 2AZ, United Kingdom
(Received 2 February 2016; published 1 August 2016)

The flow on the centerline of grid-generated turbulence is characterized via hot-wire anemometry for three grids with different geometry: a regular grid (RG60), a fractal grid (FSG17), and a single-square grid (SSG). Due to a higher value of the thickness t_0 of its bars, SSG produces greater values of turbulence intensity Tu than FSG17, despite SSG having a smaller blockage ratio. However, the higher Tu for SSG is mainly due to a more pronounced vortex shedding contribution. The effects of vortex shedding suppression along the streamwise direction x are studied by testing a three-dimensional configuration, formed by SSG and a set of four splitter plates detached from the grid (SSG+SP). When vortex shedding is damped, the centerline location of the peak of turbulence intensity x_{peak} moves downstream and Tu considerably decreases in the production region. For FSG17 the vortex shedding is less intense and it disappears more quickly, in terms of x/x_{peak}, when compared to all the other configurations. When vortex shedding is attenuated, the integral length scale L_u grows more slowly in the streamwise direction, this being verified both for FSG17 and for SSG+SP. In the production region, there is a correlation between the vortex shedding energy and the skewness and the flatness of the velocity fluctuations. When vortex shedding is not significant, the skewness is highly negative and the flatness is much larger than 3. On the opposite side, when vortex shedding is prominent, the non-Gaussian behavior of the velocity fluctuations becomes masked.

DOI: 10.1103/PhysRevFluids.1.044402

I. INTRODUCTION

During the past decade multiscale or fractal-generated turbulence has been widely investigated, both experimentally (see, e.g., [1–9]) and with direct numerical simulations (DNSs) (see, e.g., [10–15]). At a large distance from a perturbing grid in its turbulence decay region on the centerline, where the turbulence intensity Tu decreases along the streamwise direction, fractal square grids with blockage ratio $\sigma = 25\%$ produce higher values of Tu if compared to a regular grid with $\sigma = 34\%$ and with a similar effective mesh size M_{eff} for the same inlet velocity U_∞ and for the same dimensional distance x from the grid [16]. Laizet and Vassilicos [14] performed DNSs of the flow downstream of fractal grids and of regular grids with comparable σ and similar M_{eff} and for a similar Reynolds number based on M_{eff}. This last study shows that when averaging the turbulence intensity over a plane parallel to the grid, for the same x this is higher for fractal grids than for regular grids downstream of the location of its peak value. However, the same study shows that upstream of the location of this maximum, the plane-averaged turbulence intensity is higher for regular grids than for fractal grids. The distance x_{peak} from the grid, where Tu is maximum on the centerline, is the streamwise extent of the turbulence production region, where Tu increases with x, and is representative of the location where the wakes, originating from the largest bars of the grid, meet on the centerline. The distance x_{peak} can be approximately predicted in terms of the wake-interaction length scale $x^* = L_0^2/t_0$ [16], where L_0 is the length of the bars of the largest iteration of the square pattern and t_0 is their thickness in a plane normal to the direction of the flow.

Gomes-Fernandes *et al.* [17] theoretically motivated and experimentally demonstrated that (i) x_{peak}/x^* is inversely proportional to the drag coefficient c_d of the largest bars of the grid and

*g.melina13@imperial.ac.uk

(ii) the value of Tu at x_{peak}, Tu_{peak}, is proportional to $c_d t_0/L_0$. The latter result suggests that we can use a grid made of a single square [18] designed with a large ratio t_0/L_0, so that Tu is high while σ, and presumably also the static pressure drop, is small.

Fractal geometries have proved to be an effective solution for suppressing vortex shedding downstream of particular objects. In axisymmetric turbulent wakes produced by fractal plates, the vortex shedding energy is reduced by up to 60% compared to the case of circular and square plates with the same frontal area [7]. Nedić and Vassilicos [19] showed that by increasing the number of fractal iterations in an airfoil's (NACA 0012) trailing edge with multiscale modifications, the energy of vortex shedding decreases too. It is believed that the fractal modification of the perimeter affects the vortex shedding formation mechanism and redistributes the turbulent kinetic energy among a broader range of scales (frequencies).

Mazellier and Vassilicos [16] discovered that, downstream of fractal square grids, strong rare decelerating flow events occur in the turbulence production region. As a result, the probability density functions of the velocity fluctuations u appear highly left skewed and characterized by large values of flatness. On the contrary, advancing further downstream in the turbulence decay region, the skewness and the flatness of u gradually get close to values typical of a Gaussian distribution. These observations lead to some new research questions. (i) Are these features typical of fractal grids or are they also observable with regular and single-scale grids? (ii) Which phenomena can affect the magnitude of these events, given in particular that in the turbulence production region the wakes shed from the largest bars of the grid have not fully met yet. (iii) Does vortex shedding play a significant role in the production region, especially when the value of t_0 is considerably high? (iv) If yes, how are the statistics of the velocity fluctuations affected by the vortex shedding energy content? (v) Is vortex shedding attenuated in the production region of fractal grids, as a result of the presence of the smaller geometrical iterations?

The aim of this paper is to provide some answers to these research questions. We first characterize the flow downstream of three types of turbulence-generating grids placed in a wind tunnel. We consider a regular grid (RG60), a fractal square grid (FSG17), and a single-square grid (SSG) with the highest value of t_0/L_0. We perform single-component hot-wire measurements downstream of the grids, mainly on the centerline. We also quantify the static pressure drop along the centerline by traversing a Pitot-static tube. We focus on some of the effects induced by the vortex shedding originating from the largest bars of the grids. For this purpose we also consider a three-dimensional turbulence generator (SSG+SP) that is formed by SSG and a set of four splitter plates detached from it.

It is well known that, among passive techniques, vortex shedding suppression by using splitter plates is one of the simplest and most effective solutions [20]. Roshko [21] showed that, when a long splitter plate is attached downstream of a circular cylinder with diameter D, c_d is reduced as a result of the vortex shedding suppression. Apelt and West [22] performed experiments on splitter plates past bluff bodies and investigated the effect of L_{sp}, where L_{sp} is the length of the splitter plate. They found that regular vortex shedding is completely suppressed when the reattachment of the flow occurs on the splitter plate. This happens for $L_{sp}/D \geqslant 3$ for a plate normal to the flow and for $L_{sp}/D \geqslant 5$ for a circular cylinder. This last result also holds for a splitter plate attached to a rectangular prism, as shown in Ref. [23]. However, when long splitter plates are used, a well-developed vortex street arises from the combined bluff-body–splitter plate. Vortex shedding can also be reduced using a shorter detached splitter plate placed at a distance x_{sp} from the bluff body, where x_{sp} is measured until the splitter plate's leading edge. Roshko [21] found that by using a splitter plate with $L_{sp}/D = 1.14$ detached from a circular cylinder at $\text{Re}_D = 14\,500$, an optimal position exists for which vortex shedding attenuation is maximum and c_d is minimum; Re_D is the Reynolds number based on D. This optimum occurs for $x_{sp}/D = 2.7$. Similar results were obtained by performing DNS at lower Re_D. Lin and Wu [24] found an optimal distance $x_{sp}/D = 2.5$ for $L_{sp}/D = 2$ and $\text{Re}_D = 100$ and Hwang *et al.* [25] reported an optimal value $x_{sp}/D = 2.7$ for $L_{sp}/D = 1$ and $\text{Re}_D = 160$.

In this work we identify an optimal distance x_{sp}/t_0 between the splitter plates and SSG from a limited number of such distances that we have been able to experiment with. We estimate the energy associated with a band of frequencies centered on the vortex shedding frequency (vortex shedding

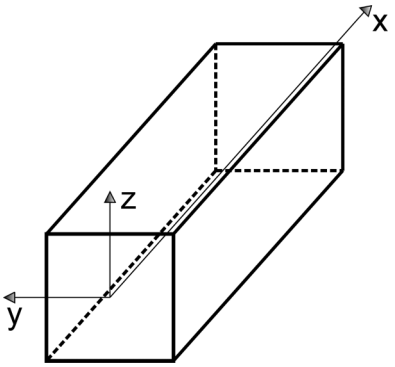

FIG. 1. Sketch of the wind tunnel's test section.

energy) for the configuration with and without splitter plates. We quantify the vortex shedding energy content for FSG17 and we compare it to SSG and SSG+SP at the same values of x/x_{peak} along the centerline. We highlight the effects of the vortex shedding attenuation. In particular we study how the vortex shedding energy affects the skewness and the flatness of the velocity fluctuations in the turbulence production region.

The remainder of this paper is structured as follows. In Sec. II we describe the experimental technique and the data reduction process. In Sec. III we characterize the turbulent flow for RG60, FSG17, and SSG. In Sec. IV we discuss the effects of vortex shedding suppression along the centerline. We summarize in Sec. V.

II. EXPERIMENTAL DETAILS

A. Wind tunnel

Experiments have been performed in a low-speed open-loop wind tunnel. Its maximum velocity, when empty, is 33 m/s with a background turbulence intensity of 0.1%. The working section is 3 m long with a square cross section $T^2 = 0.46^2$ m^2. A sketch of the wind tunnel's test section is shown in Fig. 1 in order to define the spatial coordinate notation used in this paper. The inlet velocity U_∞ upstream of the grid is imposed by measuring the static pressure difference across the wind tunnel's contraction with a micromanometer Furness Control FCO510. In the present measurements 5 m/s $\leqslant U_\infty \leqslant$ 17 m/s. The boundary layer displacement thickness in the empty wind tunnel (no grids at the inlet) is estimated to be lower than 10 mm at $x = 3$ m for the minimum U_∞, $U_\infty = 5$ m/s. The temperature of the flow is measured with a thermocouple placed at the inlet of the test section and the ambient pressure is measured with an absolute pressure gauge connected to the micromanometer.

B. Turbulence-generating grids

In this work, three different turbulence-generating grids are placed at the inlet ($x = 0$) of the wind tunnel's test section. The grids extend over the entire size of the cross section of the wind tunnel. Scaled diagrams of the grids are illustrated in Fig. 2. The first grid is a regular biplanar grid (RG60) that has a blockage ratio $\sigma = 32\%$. The second grid is a multiscale fractal square grid (FSG17) that has been widely studied and documented in several previous experiments (see [1,2,16,18,26,27]). This grid has four iterations ($N = 4$) and $\sigma = 25\%$. The thickness ratio is $t_r = t_0/t_{N-1} = 17$, where t_{N-1} is the thickness of the smallest bars. The ratio of the lengths of the bars of two successive iterations is $R_L = L_{j+1}/L_j = 0.5$ and the ratio of their thickness is $R_t = t_{j+1}/t_j = t_r^{1/(1-N)} = 0.39$ ($j = 0,1,2$). Finally, the third grid is a single-square grid (SSG) with $\sigma = 20\%$. This is a single-scale grid and it is simply made of one thick square supported by eight thin struts (6 mm thick). The SSG

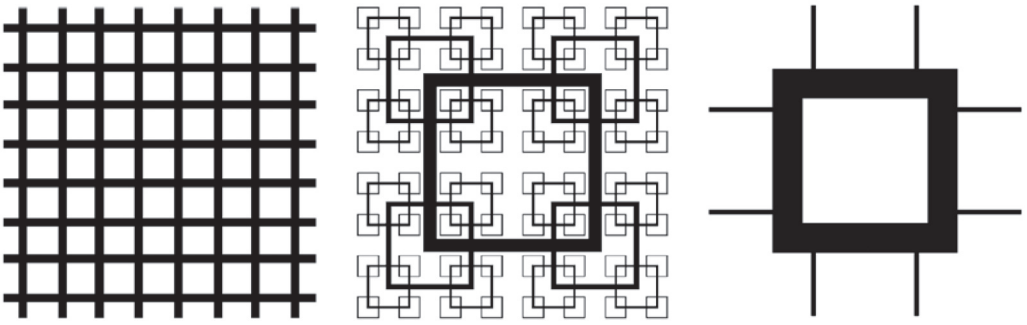

FIG. 2. Turbulence-generating grids used in the experiments: (a) RG60, (b) FSG17, and (c) SSG.

is designed to obtain high values of Tu while keeping low values of σ, i.e., increasing the ratio t_0/L_0, but still allowing a sufficiently high value of x^* in order to generate an extended turbulence production region.

The geometrical details of the grids and the inlet Reynolds numbers based on t_0, $\mathrm{Re}_{t_0} = U_\infty t_0/\nu$, are summarized in Table I; ν is the kinematic viscosity of air. We report the sectional drag coefficients c_d of the largest bars of the grids, which are estimated by interpolating the experimental values collected in Ref. [28] as a function of the aspect ratio c_0/t_0, where c_0 is the depth of the bars in the x direction (chord).

C. Splitter plates

The primary goal of this paper is to assess the importance of vortex shedding in the production region of grid-generated turbulence. Given that SSG is the grid with the largest value of t_0, we expect that the effect of vortex shedding will be most pronounced in its production region. For this reason we design a static device to be placed downstream of SSG in such a way that the vortex shedding mechanism is attenuated, allowing an assessment of the grid behavior with different levels of intensity of vortex shedding.

This is a set of four splitter plates that, when connected together, form an open box where the distance between two parallel plates matches the value of L_0, therefore every element is aligned along the median line of the bars of SSG (see Fig. 3). The length of the splitter plates in the x direction is $L_{sp} = 64.5$ mm, so $L_{sp}/t_0 = 1.5$. The thickness of the plates is $t_{sp} = 5$ mm and the ratio t_{sp}/t_0 is 0.116. For a circular cylinder with diameter D at $\mathrm{Re}_D = 5\,500$, no appreciable differences were found in the experimental results of Akilli *et al.* [20], who used splitter plates with three different thickness ratios ($t_{sp}/D = 0.016, 0.04, 0.08$). The turbulence intensity downstream of the splitter plates (without the presence of grids at the inlet of the wind tunnel) does not exceed 0.25% for $0 < x < 2.3$ m on the centerline.

The plates are connected to an outer square frame due to eight supporting struts aligned with those supporting SSG. The distance x_{sp} between the leading edge of the splitter plates and the grid can be freely varied. Preliminary measurements were made with values of x_{sp}/t_0 between 0 and 5 in order to

TABLE I. Geometrical parameters of the grids and inlet Reynolds numbers Re_{t_0} for $U_\infty = 5$–17 m/s.

Grid	L_0 (mm)	t_0 (mm)	x^* (mm)	c_0/t_0	c_d	σ (%)	Re_{t_0}
RG60	60.0	10.0	360.0	1.00	2.14	32	3310–11260
FSG17	237.8	19.2	2945.3	0.32	2.25	25	6360–21620
SSG	229.0	43.0	1219.6	0.13	2.01	20	14240–48410

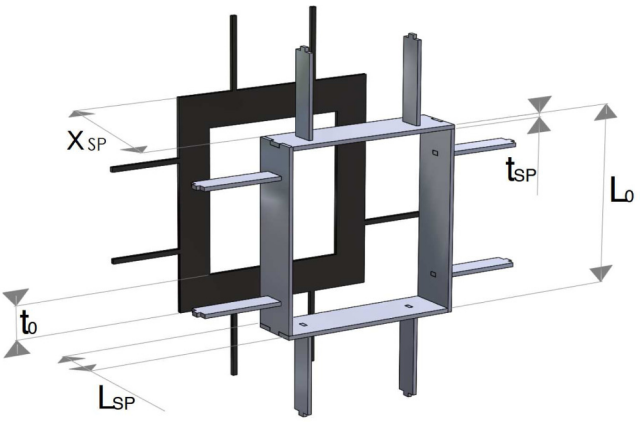

FIG. 3. Sketch of SSG with splitter plates (SSG+SP).

identify an optimal distance at which the splitter plates are most effective. In this paper we henceforth refer to the configuration formed by SSG and the set of splitter plates as SSG+SP (see Fig. 3).

D. Velocity and pressure measurements

Velocity measurements have been performed via single-component hot-wire anemometry. The hot wire is made from a Wollaston wire with a 5-μm-diam d_w platinum core that is soft soldered on a Dantec 55P01 hot-wire probe. The wire sensing element is obtained by etching its central part with a nitric acid bath. The resulting sensing length is about 1 mm long (l_w), thus giving an aspect ratio l_w/d_w of about 200. The hot-wire probe is mounted on a Dantec 55H21 support coupled to a traverse system that allows movement along the x and the z directions. The hot-wire probe is operated by a Dantec Streamline Pro constant-temperature anemometer system. The hot wire is systematically calibrated before and after each experimental run against the free-stream velocity of the wind tunnel. The calibrations are obtained using fourth-order polynomial fits of the velocity as a function of the voltage at constant temperature. The conditioned signal is sampled at 100 kHz, with the analog low-pass filter on the Streamline set at 30 kHz, using a National Instruments-6229 data acquisition system connected to a computer. The hot-wire measurements are performed at $U_\infty = 5$ and 17 m/s for all the grids. Moreover, for the comparison between SSG and SSG+SP, measurements are also performed at an intermediate velocity $U_\infty = 11$ m/s. In order to obtain converged statistics, the sampling time for each measurement point on the centerline is set to 300 s, which corresponds to at least 29 000–97 000 integral time scales for the minimum and maximum U_∞, respectively. The sampling time for the measurements relative to the vertical velocity profiles (along z) is reduced to 120 s since in this case we are only interested in low-order statistics (mean velocity and turbulence intensity).

The Reynolds decomposition of the instantaneous velocity signal $\tilde{u}(t)$ is $\tilde{u}(t) = U + u(t)$, where U is the time-averaged value $U = \langle \tilde{u}(t) \rangle$ and $u(t)$ is the fluctuating component. The turbulence intensity Tu is computed with $\mathrm{Tu} = u'/U$, where u' is the root-mean-square value of $u(t)$, $u' = \sqrt{\langle u(t)^2 \rangle}$. The longitudinal integral time scale Θ is calculated from the power spectrum density $E_u(f)$ of $u(t)$ in the frequency domain f as [29]

$$\Theta = \frac{E_u(0)}{4u'^2}. \tag{1}$$

The longitudinal integral length scale (correlation length scale) L_u is obtained from Θ by applying Taylor hypothesis, $L_u = \Theta U$. As previously done in Ref. [26] and in Ref. [16], the kinetic energy dissipation rate per unit mass ε is estimated from

$$\varepsilon = 15\nu \left\langle \left(\frac{\partial u}{\partial x} \right)^2 \right\rangle, \tag{2}$$

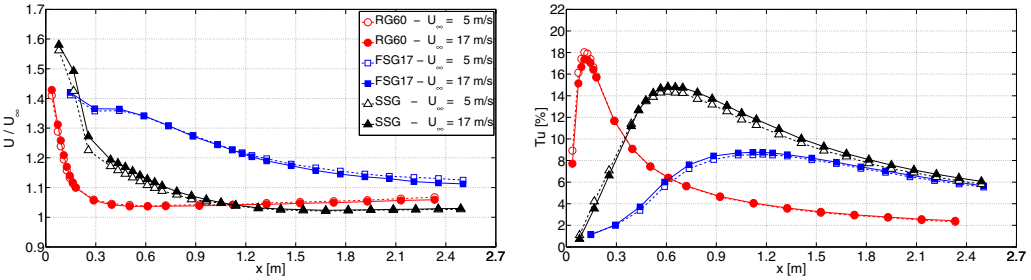

(a) (b)

FIG. 4. (a) Mean velocity and (b) turbulence intensity for RG60, FSG17, and SSG along the centerline.

where

$$\left\langle \left(\frac{\partial u}{\partial x} \right)^2 \right\rangle = \int_0^{+\infty} k^2 E_u(k) dk \tag{3}$$

under the assumption of isotropy for the small scales, which is shown to hold by the results of DNS of turbulent flows downstream of similar grids [18]. Frequencies f and $E_u(f)$ are converted to wave numbers k and $E_u(k)$ by means of Taylor hypothesis: $k = 2\pi f/U$ and $E_u(k) = U E_u(f)/2\pi$. The Taylor microscale λ is evaluated using its isotropic definition $\lambda^2 = 15\nu u'^2/\varepsilon$, the Kolmogorov length scale η is computed from $\eta = (\nu^3/\varepsilon)^{1/4}$, and the dissipation coefficient C_ε is evaluated from $C_\varepsilon = \varepsilon L_u / u'^3$.

For the hot-wire measurements performed at $U_\infty = 5$ m/s, the frequency response of the hot wire is high enough to resolve the dissipation spectrum $k^2 E_u(k)$ up to $k\eta = 1$ and above. For the measurements relative to SSG and SSG+SP at $U_\infty = 11$ m/s, the maximum resolvable $k\eta$ is at worst $k\eta \approx 0.75$, therefore the dissipation is in this case slightly underestimated (up to 2%). When considering instead the measurements performed at $U_\infty = 17$ m/s, the resolution is considerably reduced up to $k\eta \approx 0.3$ for RG60, $k\eta \approx 0.65$ for FSG17, $k\eta \approx 0.5$ for SSG, and $k\eta \approx 0.6$ for SSG+SP at worst. Taking as a reference the measurements at our lowest free-stream velocity, we estimate that for $U_\infty = 17$ m/s the values of ε would be underestimated by up to 22% for RG60, 3% for FSG17, 7% for SSG, and 4% for SSG+SP. Given the figures above, in the present paper we do not consider any results derived from ε (such as λ and C_ε) for the measurements performed at $U_\infty = 17$ m/s.

Static pressure measurements are performed along the centerline by traversing a straight Pitot-static tube downstream of the grids for $U_\infty = 5$–17 m/s. The difference between the local static pressure p (from the Pitot-static port) and the free-stream static pressure p_∞ (from pressure taps located upstream of the grids) is acquired using a second micromanometer. The pressure drop coefficient $C_{\Delta p}$ is evaluated from

$$C_{\Delta p} = \frac{p - p_\infty}{\frac{1}{2}\rho U_\infty^2}, \tag{4}$$

where ρ is the density of air at the ambient pressure and at the fluid temperature.

III. FLOW DOWNSTREAM OF THE GRIDS

A. Basic flow documentation

Figure 4 shows the normalized mean velocity U/U_∞ and the turbulence intensity Tu along the centerline downstream of RG60, FSG17, and SSG. For all three cases the mean velocity is a maximum close to the grid and successively decreases towards U_∞ proceeding further downstream. For RG60 the mean velocity is found to increase slightly with x for $x > 0.6$ m, owing to the growth of a turbulent boundary layer on the wind tunnel walls (see Appendix A). For FSG17 the mean velocity

remains considerably higher than U_∞ (about 10%) even far from the grid if compared to both RG60 and SSG. This observation for FSG17 is in good agreement with the values previously reported in Ref. [16]. For SSG the normalized mean velocity is found to be slightly lower for $U_\infty = 5$ m/s in the interval $0 < x < 1$ m. However, advancing further downstream, the values of U/U_∞ collapse with the results relative to $U_\infty = 17$ m/s.

For RG60 the turbulence intensity is high in the region close to the grid, reaching a peak value $\mathrm{Tu}_{\mathrm{peak}}$ of about 18% at $x_{\mathrm{peak}} = 0.11$ m, before rapidly dropping with downstream distance to below 5% for $x > 0.9$ m. For FSG17 and SSG the value of $\mathrm{Tu}_{\mathrm{peak}}$ is lower, about 9% for FSG17 and 15% for SSG, and it occurs for a larger distance from the grid, $x_{\mathrm{peak}} = 1.18$ m for FSG17 and $x_{\mathrm{peak}} = 0.61$ m for SSG. The latter feature is a direct result of the greater values of the wake-interaction length scale for FSG17 and SSG. The position x_{peak} can be expressed as $x_{\mathrm{peak}} = k_1 c_d^{-1} x^*$, where k_1 is a factor depending on the free-stream (upstream of the grids) turbulence intensity and on the geometry of the grid [17]. The factor k_1 is close to 0.9 for a laminar free stream (as is the case for the present measurements) and fractal grids with $\sigma = 25\%$ and with $t_r = 8,13,17$ [17]. In our measurements we find $x_{\mathrm{peak}}/x^* = 0.3,0.4,0.5$ for RG60, FSG17, and SSG respectively, therefore the corresponding values of k_1 are 0.64, 0.9, and 1. The difference in the values of k_1 between FSG17 and SSG can be attributed to the difference between the blockage ratios of the two grids [30]. Laizet *et al.* [18] have experimental evidence where x_{peak}/x^* is a decreasing function of σ. The value of k_1 is found to be significantly lower for RG60. This difference might be due both to the higher blockage ratio of RG60 and also to the fact that, differently from FSG17 and SSG, this grid is regular and biplanar. This is in agreement with the observations made in Ref. [17], where the value of k_1 for the fractal grids used in their experiment was found to be higher than that for the regular square-mesh grids used in Ref. [31].

In the turbulence production region and close to x_{peak} the values of Tu for SSG, which has the lowest σ, are considerably higher if compared to FSG17. The reason for this is related to the higher ratio t_0/L_0 for SSG, which is more than double that for FSG17. Note that the values of turbulence intensity for a fractal square grid are higher than those for a single-square grid with the same t_0/L_0 [13]. The physical argument that can explain the nature of the higher turbulence intensity in the production region of our SSG is further discussed in Sec. IV. In the turbulence decay region, the values of Tu for FSG17 approach those for SSG, both being considerably higher than those for RG60.

Figure 5 shows vertical profiles of U and Tu (normalized by their value on the centerline) for $0 \leqslant z/L_0 \leqslant 0.5$, at a series of streamwise locations in the turbulence decay regions of the grids. It is clear that the mean velocity profiles become more homogeneous as one moves downstream and that RG60 seems to reach the best level of homogeneity when compared to the other grids, with its profiles becoming completely flat at $x \geqslant 0.72$ m. However, one must consider that x^* (and so x_{peak}) is substantially smaller for RG60. Therefore, if we made a comparison at the same x, we would not be taking into account that the flow is much further away from its production region for this grid than for FSG17 and SSG. In fact, the position $x = 0.72$ m corresponds to $x/x_{\mathrm{peak}} = 6.67$ for RG60, which is a value that we never reach for either FSG17 or SSG in the present wind tunnel. A similar observation can be made when comparing the homogeneity of the mean velocity between FSG17 and SSG. If we compare the profiles for FSG17 at $x = 2.21$ m (or $x = 2.50$ m) with the ones for SSG at $x = 2.22$ m (or $x = 2.49$ m), we conclude that the mean velocity downstream of SSG is more homogeneous. On the contrary, when we compare the profiles measured at the same x/x_{peak}, for example, $x/x_{\mathrm{peak}} = 1.87$ for both FSG17 and SSG, we instead conclude that FSG17 and SSG exhibit the same level of homogeneity since $U_{z/L_0=0.5}/U_{z/L_0=0}$ is about 0.93 for FSG17 and 0.91 for SSG.

When comparing the vertical profiles of Tu in Fig. 5 we notice that FSG17 differs from the other two grids. For both RG60 and SSG the turbulence intensity is a monotonically increasing function of z for $0 \leqslant z/L_0 \leqslant 0.5$. On the contrary, for FSG17 the profiles of Tu exhibit a local maximum around $z/L_0 = 0.25$. This feature is most probably due to the presence of the smaller geometrical iterations on the fractal square grid. We observe that $z/L_0 = 0.25$ is the coordinate where the profiles of the mean velocity for FSG17 and RG60 show an inflection point, i.e., $(\partial^2 U/\partial z^2)_{z/L_0=0.25} = 0$. If we now reasonably assume that $|\partial U/\partial z| \gg |\partial W/\partial x|$ (and $|\partial U/\partial y| \gg |\partial V/\partial x|$), for FSG17 the position where Tu is maximum corresponds to the location where the absolute value of the

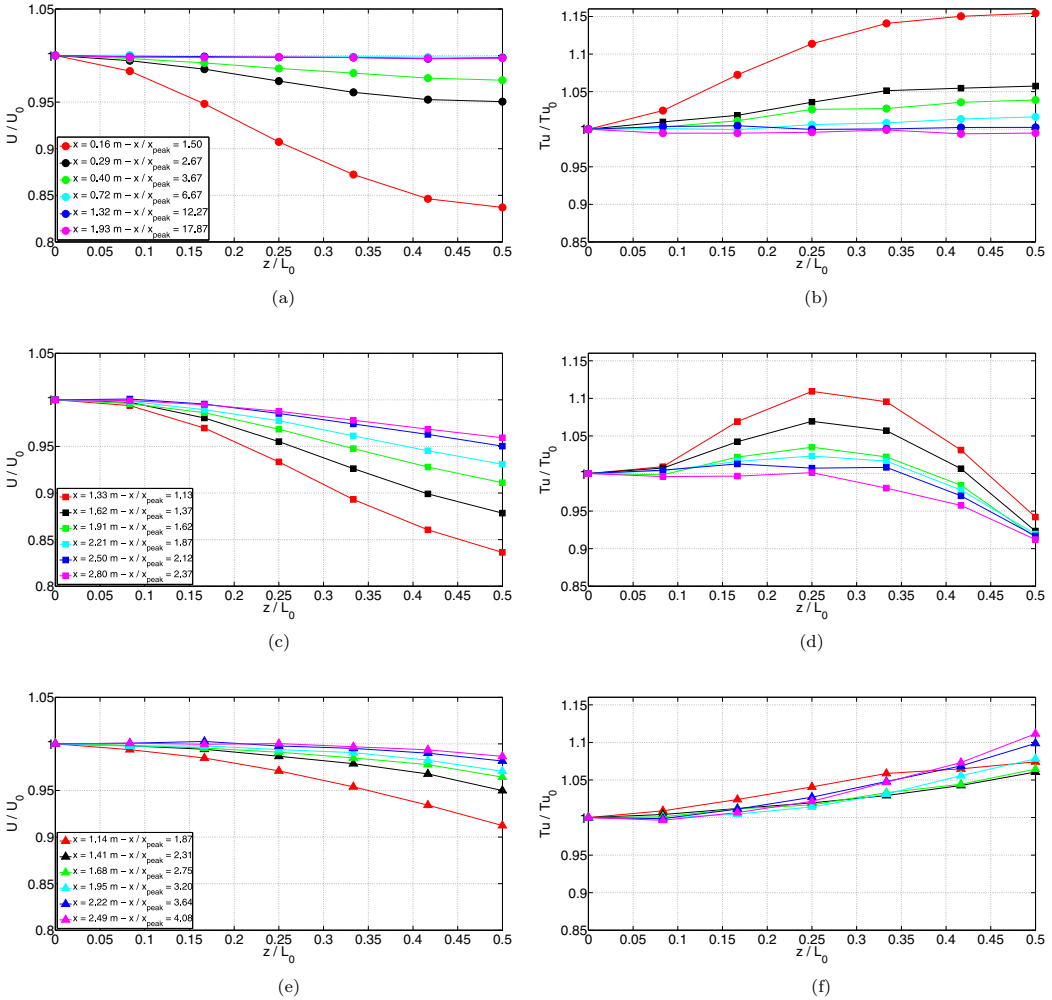

FIG. 5. Vertical profiles of mean velocity (left column) and turbulence intensity (right column) for (a) and (b) RG60, (c) and (d) FSG17, and (e) and (f) SSG. U_0 and Tu_0 are, respectively, the mean velocity and the turbulence intensity on the centerline; $U_\infty = 17$ m/s.

y component (or alternatively of the z component for symmetry considerations) of the mean vorticity, $\partial U/\partial z - \partial W/\partial x \approx \partial U/\partial z\,(\partial V/\partial x - \partial U/\partial y \approx -\partial U/\partial y)$, is also maximum.

The pressure drop coefficient $C_{\Delta p}$ along the centerline is plotted against x and x/x_{peak} in Fig. 6 for the three grids. The absolute value of $C_{\Delta p}$ in the far decay region is maximum for RG60 whereas it is minimum for SSG, consistently with the decreasing blockage ratio of the grids. On the other hand, the pressure recovery length, that is, the distance after which the pressure should remain constant, is the highest for SSG. We have to remark that in our case the pressure drop coefficient does not reach a well-defined constant value but it is found to slightly decrease along x. This can be explained by the growth of the boundary layer on the walls of the wind tunnel (the mean velocity increases and the static pressure decreases). We notice that for SSG the values of $C_{\Delta p}$ are notably higher for $U_\infty = 5$ m/s than for $U_\infty = 17$ m/s in the interval $0 < x < 1$ m ($0 < x/x_{\mathrm{peak}} < 1.65$), which coincides with the region where we have observed a lower mean velocity [see Fig. 4(a)].

Figure 7(a) shows the evolution of the longitudinal integral length scale L_u along the centerline for the different grids, where L_u has been normalized with the tunnel width T. For each of the

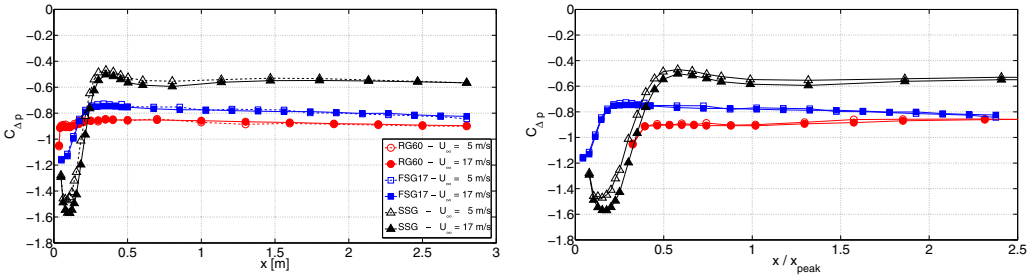

(a) (b)

FIG. 6. Pressure drop coefficient as a function of (a) x and (b) x/x_{peak} for RG60, FSG17, and SSG along the centerline.

three grids there is a satisfactory collapse of the measurements taken at two different free-stream velocities, indicating that L_u is invariant with U_∞, at least for the range investigated in this study. This means that the downstream evolution of this length scale is set by the geometry of the grids only and not by the inlet Reynolds number. For FSG17 and SSG, the very first measurement positions in the turbulence production region are characterized by large values of L_u since the flow is still intermittent there (L_u is much larger in a laminar flow than in a turbulent one). Advancing further downstream in the turbulence decay regions, the values of L_u are considerably lower for RG60 due to the fact that L_0 is smaller for RG60 than for FSG17 and SSG. These two grids have very similar L_0 and consequently comparable values of L_u. However, FSG17 exhibits the slowest growth of L_u with x, similarly to what was originally observed in Ref. [1]. It is interesting to look at the ratio between the integral and the Taylor length scales L_u/λ [Fig. 7(b)], which gives an indication of the separation between the large and the small scales of the turbulent fluctuations. In the region where C_ε is constant for fixed inlet conditions, the ratio L_u/λ should decrease in proportion to Re_λ, where

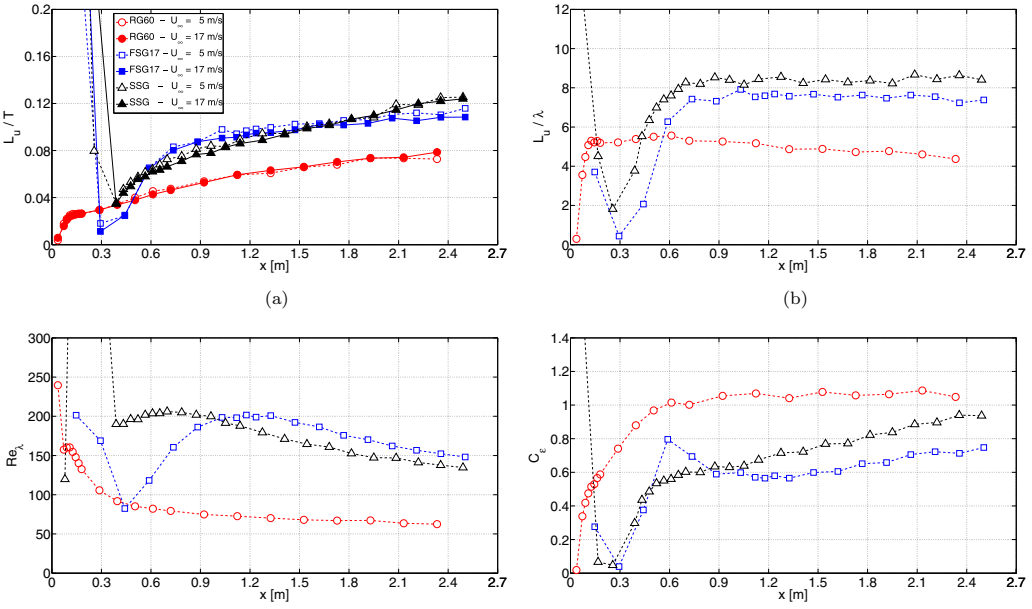

(a) (b) (c) (d)

FIG. 7. (a) Integral length scale, (b) ratio between integral and Taylor length scales, (c) Reynolds number based on Taylor length scale, and (d) dissipation coefficient for RG60, FSG17, and SSG along the centerline. Data for $U_\infty = 17$ m/s are not shown for quantities derived from ε as explained in Sec. II D.

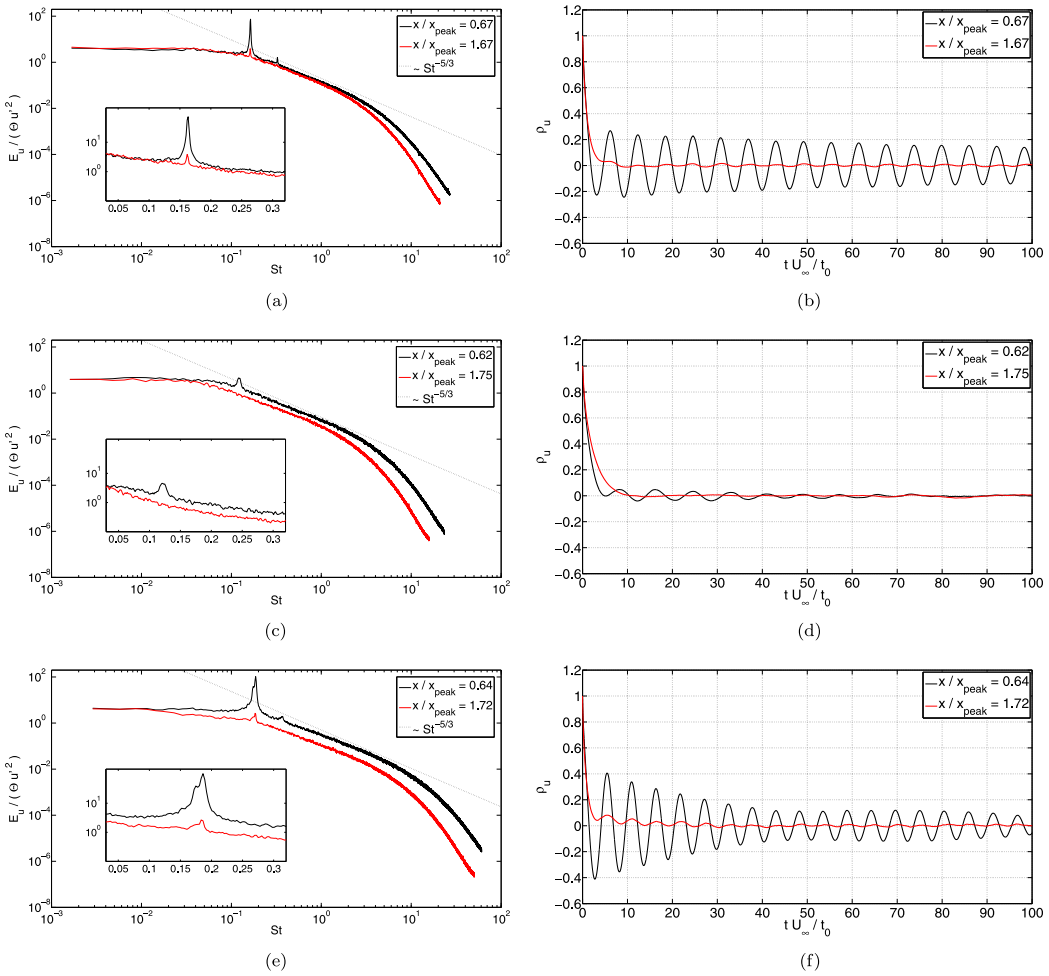

FIG. 8. Power spectrum density (left column) and autocorrelation coefficient (right column) of u in the production region (black) and in the decay region (red) of (a) and (b) RG60, (c) and (d) FSG17, and (e) and (f) SSG on the centerline; $U_\infty = 5$ m/s.

$\mathrm{Re}_\lambda = u'\lambda/\nu$. A comparison of the plots in Figs. 7(b) and 7(c) shows that this feature holds for RG60 when $x > 0.6$ m ($x/x_{\mathrm{peak}} > 5.5$), where C_ε [Fig. 7(d)] approaches a constant value. On the contrary, for FSG17, as already previously discussed in Ref. [26], in the turbulence decay region the ratio L_u/λ remains approximately constant, despite Re_λ clearly decreasing. Here we show that the same feature can be also observed for SSG. This indicates that, for both FSG17 and SSG, our measurements are always performed in the nonequilibrium region of turbulence where $C_\varepsilon \neq$ const. In this region $C_\varepsilon \propto \mathrm{Re}_\lambda^{-1}$, which implies $L_u/\lambda =$ const for fixed inlet conditions.

B. Production region

We make a comparison between two streamwise positions on the centerline, one in the production region ($x/x_{\mathrm{peak}} < 1$) and the other in the decay region ($x/x_{\mathrm{peak}} > 1$). The positions have been chosen to give similar values of x/x_{peak} for each grid: $x/x_{\mathrm{peak}} = 0.67, 0.62, 0.64$ in the production region and $x/x_{\mathrm{peak}} = 1.67, 1.75, 1.72$ in the decay region for RG60, FSG17, and SSG, respectively.

In Figs. 8(a), 8(c), and 8(e) we show the power spectrum density E_u for the measurements taken at $U_\infty = 5$ m/s. Frequencies have been converted to Strouhal numbers St using a reference frequency

TABLE II. Vortex shedding Strouhal numbers St_{sh} and St_{sh}^{A} for RG60, FSG17, and SSG; $U_\infty = 5$ and 17 m/s.

	St_{sh}		St_{sh}^{A}	
U_∞ (m/s)	5	17	5	17
RG60	0.163	0.167	0.399	0.409
FSG17	0.125	0.126	0.440	0.443
SSG	0.187	0.189	0.432	0.436

given by U_∞/t_0 and the energy density has been normalized with $\Theta u'^2$. For each spectrum the cutoff frequency is chosen to be $f_{\mathrm{cut}} = 1.2 f_\eta$, where f_η is the Kolmogorov frequency $f_\eta = U/2\pi\eta$. In the inertial range all the spectra exhibit a Kolmogorov-like power law decay $E_u \sim \mathrm{St}^{-p}$, with p close to 5/3, both in the production region and in the decay region. For all the grids, in the production region the inertial range is observable for higher frequencies and it is more extended than for the decay region, in agreement with the recent observations made in Ref. [18]. In addition to this, the extent of the inertial range is larger for FSG17 and SSG than for RG60.

In the production region the spectra corresponding to RG60 and SSG show a clear peak that is due to the presence of vortex shedding from the bars of the grids. The intensity of this peak gets attenuated as one proceeds downstream in the decay region but, at the considered locations, it is still detectable for both RG60 and SSG. If we now consider the case of FSG17, in the production region the vortex shedding phenomenon seems to be less pronounced when compared to both RG60 and SSG at similar values of x/x_{peak}. Furthermore, for FSG17 the effect of vortex shedding is not even detectable in the turbulence decay region, in contrast to both RG60 and SSG at the same values of x/x_{peak}. We return to this point in Sec. IV of this paper. The effect of vortex shedding can also be detected by directly looking at the autocorrelation coefficient ρ_u of u, which is plotted in Figs. 8(b), 8(d), and 8(f), where the time t has been normalized by the reference time scale t_0/U_∞. In the production region the coefficient ρ_u exhibits a periodic behavior that is damped for large t and, in agreement with the previous considerations, this periodic behavior is much less marked for FSG17. It is interesting to notice how, in the decay region, ρ_u smoothly decays to zero with no sign of periodicity for FSG17, unlike RG60 and SSG.

The vortex shedding Strouhal numbers based on t_0, $\mathrm{St}_{sh} = f_{sh} t_0/U_\infty$, are reported in Table II for the measurements corresponding to $U_\infty = 5$ and 17 m/s; f_{sh} is the frequency at which the spectra exhibit a consistent peak in the production region, at different locations along the centerline. We notice that St_{sh} is almost invariant with U_∞ for all three grids. The value of St_{sh} for FSG17 is considerably lower when compared to both RG60 (about 24% less) and SSG (about 33% less). We check if, by using a different reference length for the definition of the Strouhal number, it might be possible to obtain similar vortex shedding Strouhal numbers for the different grids. For this purpose we consider the reference length $l_0 = \sqrt{t_0 L_0}$, which is proportional to the square root of the area of the largest bars of the grid (and also proportional to the area covered by the entire largest square pattern iteration). This approach is similar to what was done in Ref. [32] for plates with different regular and fractal geometries, in accordance to the original idea used in Ref. [33]. We define a supplementary vortex shedding Strouhal number based on l_0, $\mathrm{St}_{sh}^{A} = f_{sh} l_0/U_\infty = \mathrm{St}_{sh}\sqrt{L_0/t_0}$. The results in Table II show that the values of St_{sh}^{A} for the different grids are considerably closer than for St_{sh}; in particular they are almost the same for FSG17 ($\mathrm{St}_{sh}^{A} \approx 0.44$) and for SSG ($\mathrm{St}_{sh}^{A} \approx 0.43$). We do not have enough data to claim the universality of St_{sh}^{A} (or some closely related Strouhal number) for grid-generated turbulence. However, we show that the percentage difference, between the maximum and the minimum value (with respect to the average value) among the three grids considered here, drops from 40.8% for St_{sh} to 9.5% for St_{sh}^{A}.

As already mentioned in the Introduction, it was experimentally shown that in the production region of fractal square grids the distributions of the velocity fluctuations are far from Gaussian; they exhibit high values of flatness and are highly left skewed [16]. In Fig. 9 we show the probability

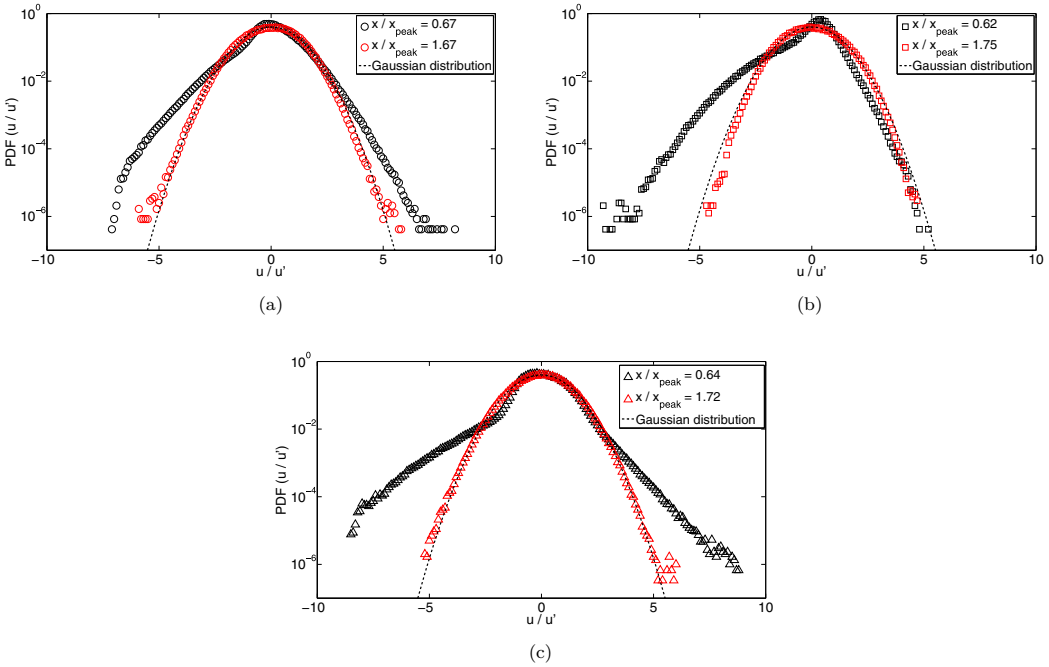

FIG. 9. Probability density functions of u in the production region (black) and in the decay region (red) of (a) RG60, (b) FSG17, and (c) SSG; $U_\infty = 17$ m/s.

density functions (PDFs) of u for RG60, FSG17, and SSG relative to the same previously considered streamwise positions (data corresponding to that plotted in Fig. 8). In the turbulence decay region the PDFs get close to a Gaussian distribution. For $x/x_{\text{peak}} \approx 1.7$ the skewness of u, $S = \langle u^3\rangle/\langle u^2\rangle^{3/2}$, is indeed near zero; $S = -0.09, 0.07, -0.04$; and the flatness $F = \langle u^4\rangle/\langle u^2\rangle^2$, close to 3, $F = 2.89, 2.81, 2.99$ for RG60, FSG17, and SSG respectively. On the opposite side, the PDFs clearly do not follow a Gaussian distribution and appear left skewed in the production region ($x/_{\text{peak}} \approx 0.64$), not only for FSG17 but also for the other two grids. The values of the skewness are indeed all negative, $S = -0.31, -1.34, -0.48$ for RG60, FSG17, and SSG respectively. The flatness exhibits values higher than 3, $F = 4.61, 5.85, 6.13$ for RG60, FSG17, and SSG, respectively.

These figures suggest that, in the production region, rare strong decelerating flow events are more likely to occur than accelerating events and this holds for three turbulence-generating grids with very different geometries. However, our results show that for FSG17 this feature (the high negative skewness) is even more pronounced when compared to both RG60 and SSG. Given that FSG17 is actually the grid where the vortex shedding signature appears to be less evident, it becomes natural to ask whether the energy associated with this periodic phenomenon affects the Gaussianity of the velocity fluctuations. The study of this aspect is addressed in the following section of this paper.

IV. VORTEX SHEDDING SUPPRESSION

We attempt to examine some effects of vortex shedding suppression on the flow past a turbulence-generating grid along the centerline. To pursue this goal we place a set of four splitter plates detached from SSG and we perform velocity measurements downstream of this new turbulence generator (SSG+SP). We stress that our main purpose is not to optimize the vortex shedding suppression. Instead, it is to study how the flow properties change when we attenuate the vortex shedding originating from the large bars of the grid.

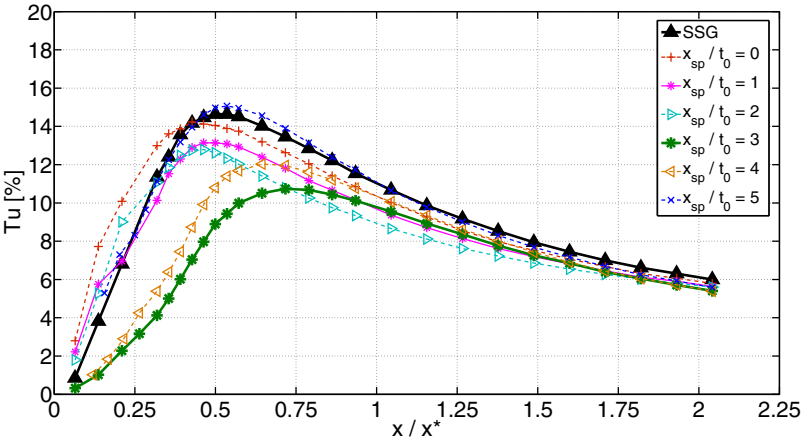

FIG. 10. Turbulence intensity for SSG and SSG+SP with different values of x_{sp}/t_0 along the centerline; $U_\infty = 11$ m/s.

First we need to identify the position x_{sp} of the splitter plates for which vortex shedding is more effectively suppressed. For this purpose we consider the centerline streamwise evolution of Tu for SSG+SP for the baseline case $U_\infty = 11$ m/s (Fig. 10) with six different positions of the splitter plates, $x_{sp}/t_0 = 0,1,2,3,4,5$, and we compare it with SSG. Among the limited number of values x_{sp}/t_0 here investigated, the position $x_{sp}/t_0 = 3$ appears to be the most effective one in decreasing the vortex shedding intensity. We motivate this statement by considering two aspects: (i) For $x_{sp}/t_0 = 3$ the distance x_{peak} is maximum and (ii) the turbulence intensity at $x = x_{\text{peak}}$, Tu_{peak}, is minimum. In particular, for this position of the splitter plates, x_{peak} is increased by 44% when compared to the configuration without splitter plates, since it moves from $0.5x^*$ to $0.72x^*$. The suppression of vortex shedding causes the wakes originated from the bars of the grid to become narrower (see, e.g., [20,34,35]) and therefore we postulate that the location of the peak of turbulence intensity, which is representative of the location where the wakes meet [16], is moved downstream. This also means that the drag coefficient c_d of the bars is reduced. If we consider the scaling $x_{\text{peak}}/x^* \propto c_d^{-1}$, an increase of 44% in x_{peak}/x^* can be explained by a decrease in c_d of about 31%, which we cannot directly assess since we do not measure the drag of the bars. However, in order to check the consistency of our findings, we can additionally make use of the scaling for Tu_{peak}, $\text{Tu}_{\text{peak}} \propto c_d t_0/L_0$. By considering this last relation, we would theoretically expect that Tu_{peak} is also reduced by about 31% due to the reduction in c_d. Looking at our baseline case for SSG at $U_\infty = 11$ m/s for consistency, we find that for $x_{sp}/t_0 = 3$ the value of Tu_{peak} decreases from 0.146 to 0.107, a reduction of 27%. Moreover, $x_{sp}/t_0 = 3$ is close to $x_{sp}/D = 2.5$–2.7, which was found to be the optimal distance for suppressing vortex shedding from a circular cylinder (see [21,24,25]).

Given that $x_{sp}/t_0 = 3$ proves to be the most effective distance for suppressing vortex shedding (from the limited number of positions here tested), we now focus on this position only for the remainder of this paper and we refer to this configuration as SSG+SP3. In Fig. 11 we show the normalized mean velocity and the turbulence intensity along the centerline for SSG+SP3. One can see that both the mean velocity and the turbulence intensity profiles at $U_\infty = 11$ and 17 m/s are very well collapsed. The ratio U/U_∞ for $U_\infty = 5$ m/s is found to be slightly lower with respect to the measurements at higher inlet velocities, with a maximum difference of 3.8% at $x/x^* = 0.64$. However, the discrepancy becomes attenuated and tends to disappear as one proceeds downstream, similarly to what was found for SSG [see Fig. 4(a)]. A comparison of Fig. 4(a) (SSG) and Fig. 11(a) (SSG+SP3) shows that the mean velocity for $0.25 < x/x^* < 0.6$ ($0.3\text{ m} < x < 0.7$ m) is higher for SSG+SP3. This can be explained by the presence of the four splitter plates, which create a contraction effect and therefore an acceleration of the flow. The turbulence intensity for $U_\infty = 5$ m/s

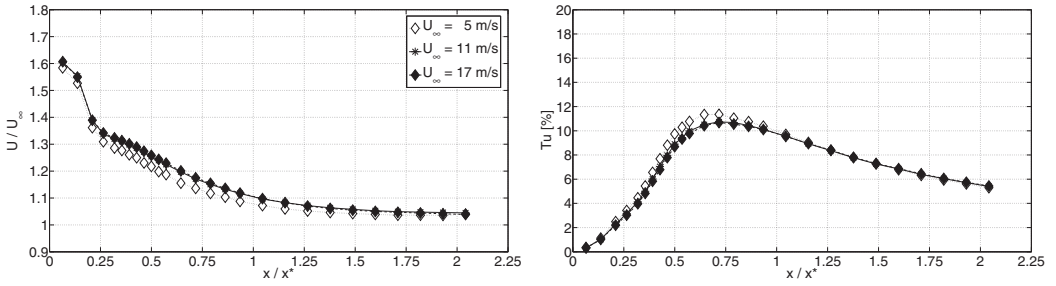

(a) (b)

FIG. 11. (a) Mean velocity and (b) turbulence intensity for SSG+SP3 along the centerline.

is marginally higher just in the proximity of x_{peak}, whose location remains the same for all the measurements performed, $x_{\text{peak}} = 0.72x^*$.

A. Vortex shedding energy

We are interested in comparing the energy related to the vortex shedding downstream of the different grids. In this work we refer to vortex shedding energy E_{sh} as the portion of the turbulent kinetic energy u'^2 that is associated with a frequency bandwidth centered around f_{sh}. In the production region, the main contribution to E_{sh} is due to vortex shedding. However, it must be noted that E_{sh} contains also part of the energy associated with the turbulent stochastic motion. The stochastic contribution can also be significant, especially past the wakes's interaction's location, given that vortex shedding occurs as a low-frequency (large scale) phenomenon.

In Fig. 12 we show the contour plots of the power spectrum density E_u for RG60, FSG17, SSG, and SSG+SP3 along the centerline for $0.35 \leqslant x/x_{\text{peak}} \leqslant 2$ and $0.04 < \text{St} < 1.1$. The values of E_u

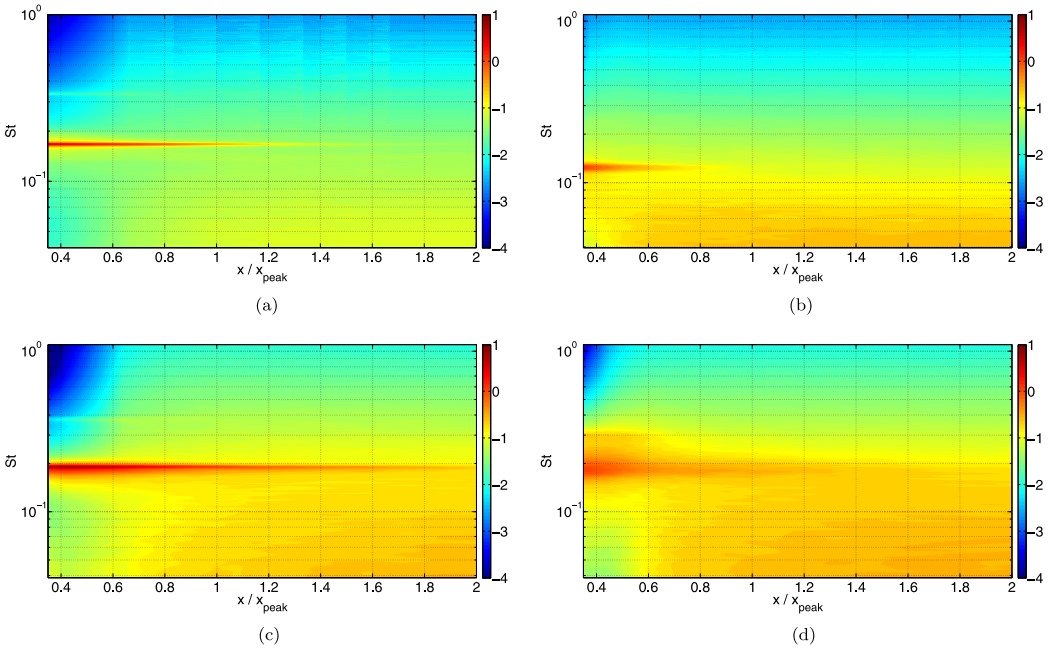

FIG. 12. Contour plots (in logarithmic scale) of the power spectrum density of u, normalized by $u'^2 T/U_\infty$, along the centerline for (a) RG60, (b) FSG17, (c) SSG, and (d) SSG+SP3; $U_\infty = 17$ m/s.

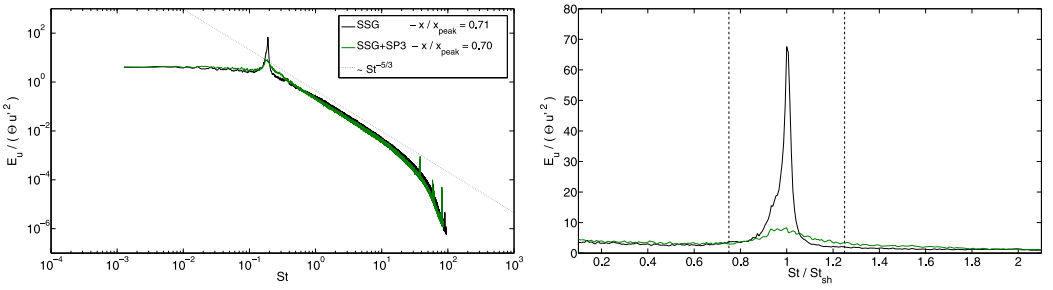

FIG. 13. Power spectrum density of u in (a) logarithmic and (b) linear scale for SSG (black) and SSG+SP3 (green) at $x/x_{\text{peak}} = 0.7$; $U_\infty = 17$ m/s. The vertical dashed lines in (b) identify the interval $\Delta\text{St}/\text{St}_{sh} = 0.5$ centered at St_{sh}.

are normalized using the local u'^2 as a reference energy and U_∞/T as a reference frequency (we do this not to contaminate the values with t_0 or L_0, which can be different for our grids). When considering the case of SSG in the production region ($x/x_{\text{peak}} < 1$), one can see that a significant contribution to the total kinetic energy comes from a narrow range of Strouhal numbers across St_{sh}, i.e., it is mainly due to vortex shedding. The signature of vortex shedding is stronger and more persistent for SSG when compared to all the other turbulence-generating grids at the same x/x_{peak}. On the opposite side the vortex shedding energy contribution to u'^2 appears to be the lowest for FSG17. Moreover, for FSG17 the effect of vortex shedding disappears more quickly in terms of x/x_{peak} as, unlike all other configurations, it is not even detectable for about $x/x_{\text{peak}} > 0.8$. Given these qualitative figures, we can already argue that the higher values of Tu for SSG with respect to FSG17 (in the production region and close to x_{peak}) can be explained physically by a more significant vortex shedding contribution.

In Fig. 13 we compare the spectra of u in the production region for SSG and SSG+SP3, specifically at $x/x_{\text{peak}} = 0.7$. By making use of $\Theta u'^2$ to normalize E_u, the spectra for the two configurations are very well collapsed with the exception of the frequency range that lies in the proximity of the vortex shedding frequency. From Figs. 12 and 13 we can observe three main effects due to the addition of the splitter plates downstream of SSG (SSG+SP3): (i) The vortex shedding contribution to u'^2 decreases, (ii) the vortex shedding signature on the centerline is less persistent, and (iii) vortex shedding appears as a more broadband phenomenon and therefore the energy is redistributed among a broader range of frequencies (scales). Given this last aspect, for SSG+SP3 it is not possible to identify a frequency f_{sh} at which a clear peak in the spectra can be observed. For this reason, in order to define a vortex shedding Strouhal number St_{sh} for SSG+SP3, we consider the frequency f_{sh} where a local energy maximum is present. With respect to SSG (see Table II), for SSG+SP3 the value of St_{sh} slightly decreases. We find $\text{St}_{sh} = 0.182$ for $U_\infty = 11$ and 17 m/s and $\text{St}_{sh} = 0.172$ for $U_\infty = 5$ m/s.

In order to give an estimate of the reduction of the vortex shedding energy due to the presence of the splitter plates, we follow the method used in Ref. [7]. We compute the vortex shedding energy E_{sh} by integrating the power spectrum density E_u for an interval of Strouhal numbers Δ St centered across St_{sh}:

$$E_{sh}(\Delta\,\text{St}) = \int_{St_1}^{St_2} E_u(\text{St})d\,\text{St}, \tag{5}$$

where $\text{St}_1 = \text{St}_{sh} - \Delta\,\text{St}/2$ and $\text{St}_2 = \text{St}_{sh} + \Delta\,\text{St}/2$. It is important to notice that the value of E_{sh} depends on the arbitrary choice of Δ St, therefore it is required to check how E_{sh} varies for different Δ St.

We quantify E_{sh} for increasing values of $\Delta\,\text{St}/\text{St}_{sh}$ and for $x/x^* \leqslant 0.72$ (extent of the production region for SSG+SP3); we use E_{sh}^I [Fig. 14(a)] to refer to the original configuration (SSG) and

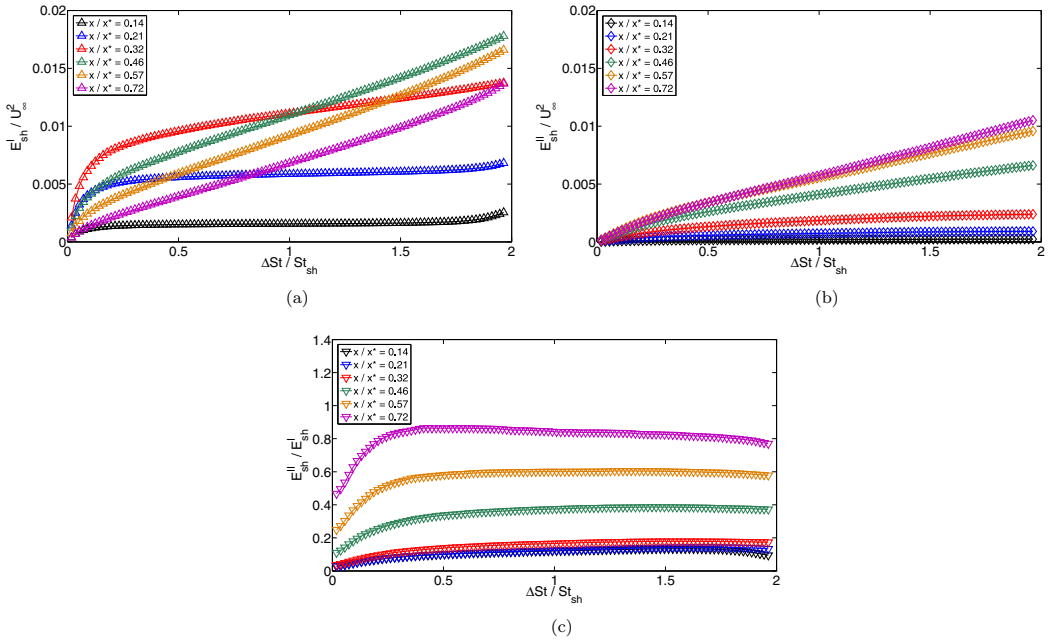

FIG. 14. Vortex shedding energy E_{sh} for (a) SSG and (b) SSG+SP3 and (c) ratio between the two varying $\Delta\mathrm{St}/\mathrm{St}_{sh}$ at different streamwise locations along the centerline; $U_\infty = 17$ m/s.

E_{sh}^{II} [Fig. 14(b)] for the configuration with the four splitter plates (SSG+SP3). The quantity E_{sh} obviously increases with Δ St according to Eq. (5). However, for the same streamwise location and for the same $\Delta\,\mathrm{St}/\mathrm{St}_{sh}$, E_{sh} is always lower for the configuration with the splitter plates. The ratio E_{sh}^{II}/E_{sh}^{I} [Fig. 14(c)] is indeed always less than 1 in the entire turbulence production region of SSG+SP3, thus confirming the vortex shedding attenuation. The reduction is greater for lower values of x, which is where vortex shedding is more prominent. It is interesting to notice that for $\Delta\,\mathrm{St}/\mathrm{St}_{sh} \gtrsim 0.5$ the ratio E_{sh}^{II}/E_{sh}^{I} remains approximately constant. This result allows us to quantify the vortex shedding suppression along the centerline without having to deal with a strong dependence on ΔSt. For this reason we choose the particular value $\Delta\,\mathrm{St}/\mathrm{St}_{sh} = 0.5$ for the integration of the power spectrum density [see Fig. 13(b)] for the comparisons in Fig. 15, where E_{sh} is taken to be $E_{sh}(\Delta\,\mathrm{St}/\mathrm{St}_{sh} = 0.5)$.

Figure 15(a) shows the evolution of E_{sh} along x/x^* for SSG and SSG+SP3. Similarly to the profiles of Tu, E_{sh} first increases with x, reaches a peak value and then subsequently decreases. For $x/x^* < 0.32$ this energy increases with a very steep gradient in the case of SSG, whereas in the same region the increase is attenuated for SSG+SP3. For $x/x^* > 0.85$ the profiles of E_{sh} for SSG and SSG+SP3 collapse. However, we have to point out that in this region the vortex shedding signature has almost disappeared; therefore, in this case E_{sh} loses the meaning of vortex shedding energy. The streamwise position where E_{sh} is maximum anticipates the peak of turbulence intensity [Fig. 15(b)] more evidently for SSG. The maximum value of E_{sh} occurs at $x/x_{\mathrm{peak}} = 0.9$ for SSG+SP3 and at $x/x_{\mathrm{peak}} = 0.7$ for SSG.

The percentage reduction of E_{sh} for SSG+SP3 (E_{sh}^{II}) with respect to SSG (E_{sh}^{I}) reaches almost 80% at $x/x_{\mathrm{peak}} = 0.45$ [Fig. 15(c)]. The reduction decreases further downstream until $x/x_{\mathrm{peak}} = 1$, where it is about 50%, and it remains approximately around this value for larger distances from the grid. The diminution of E_{sh} occurs also when compared to the total turbulent kinetic energy [Fig. 15(d)]. For $\Delta\,\mathrm{St}/\mathrm{St}_{sh} = 0.5$, the maximum value of E_{sh}/u'^2 is about 80% for SSG at $x/x_{\mathrm{peak}} = 0.42$, whereas for SSG+SP3 the maximum occurs at $x/x_{\mathrm{peak}} = 0.29$, where E_{sh}/u'^2 is about 60%. Following these positions, there exists a region until $x/x_{\mathrm{peak}} = 1$ where the ratio E_{sh}/u'^2

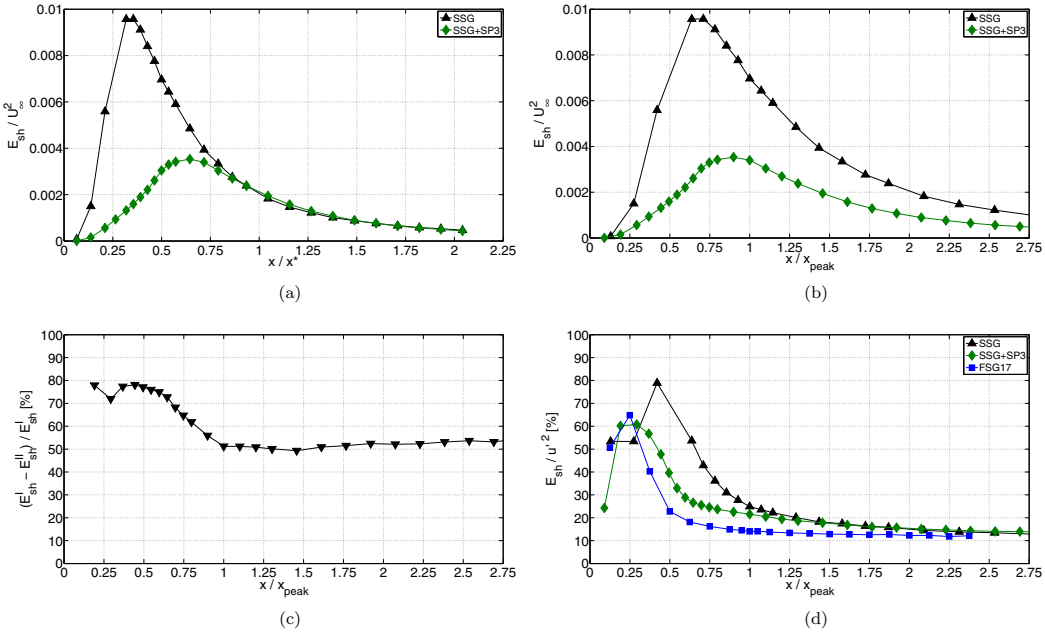

FIG. 15. Vortex shedding energy E_{sh} for SSG and SSG+SP3 as a function of (a) x/x^* and (b) x/x_{peak}, (c) percentage reduction of E_{sh} for SSG+SP3 with respect to SSG, and (d) share of turbulent kinetic energy due to vortex shedding for SSG, SSG+SP3, and FSG17; $\Delta\text{St}/\text{St}_{sh} = 0.5$ and $U_\infty = 17$ m/s.

is substantially lower for SSG+SP3. For example, at $x/x_{\text{peak}} = 0.64$ the value of this ratio is 54% for SSG and 27% for SSG+SP3. In Fig. 15(d) we also plot the ratio E_{sh}/u'^2 for FSG17 with the same choice of $\Delta\,\text{St}/\text{St}_{sh}$, i.e., $\Delta\,\text{St}/\text{St}_{sh} = 0.5$. For $x/x_{\text{peak}} > 0.35$, E_{sh}/u'^2 is considerably lower for FSG17 when compared both to SSG and to SSG+SP3. In the turbulence production region for the grid FSG17, which has $\sigma = 25\%$, the vortex shedding energy is lower than for SSG, which has almost the same L_0 and $\sigma = 20\%$, with this energy being also lower than for SSG+SP3. The interaction between wakes of different size, which occurs only with FSG17, could be an explanation for the weaker vortex shedding.

B. Effects of vortex shedding

The effects induced by the presence of the splitter plates on the downstream evolution of the turbulence length scales are examined along the centerline. The integral length scale L_u [Fig. 16(a)] takes very similar values for SSG and SSG+SP3 in the range $0.5 < x/x^* < 1$. However, when considering the turbulence decay regions, it is clearly noticeable that the growth of L_u with x is reduced for SSG+SP3. We remark that the range where this occurs ($x/x^* > 0.5$) is quite far from the splitter plates, whose trailing edge is at $x/x^* = 0.16$ for the SSG+SP3 configuration. This result is analogous to what we have observed for FSG17 (where vortex shedding is also reduced), for which the increase of L_u with x is also found to be slower than that for SSG [see Fig. 7(a)].

Similarly to L_u, the growth of the Taylor microscale λ along the streamwise direction [Fig. 16(b)] is also lower for the configuration with the splitter plates. In particular, in the decay region, $\partial\lambda/\partial x \approx \partial L_u/\partial x$ for both SSG and SSG+SP3. The last condition is actually required in order to satisfy $L_u/\lambda \approx$ const along x in the $C_\varepsilon \neq$ const region of turbulence (see [36]). We show in fact that, even when we add the splitter plates, the ratio L_u/λ remains approximately constant [Fig. 16(c)] in the region where Re_λ is decreasing [Fig. 16(d)]. Analogously, the coefficient C_ϵ [Fig. 16(e)] is not constant, but it instead increases with downstream distance in the turbulence decay region of

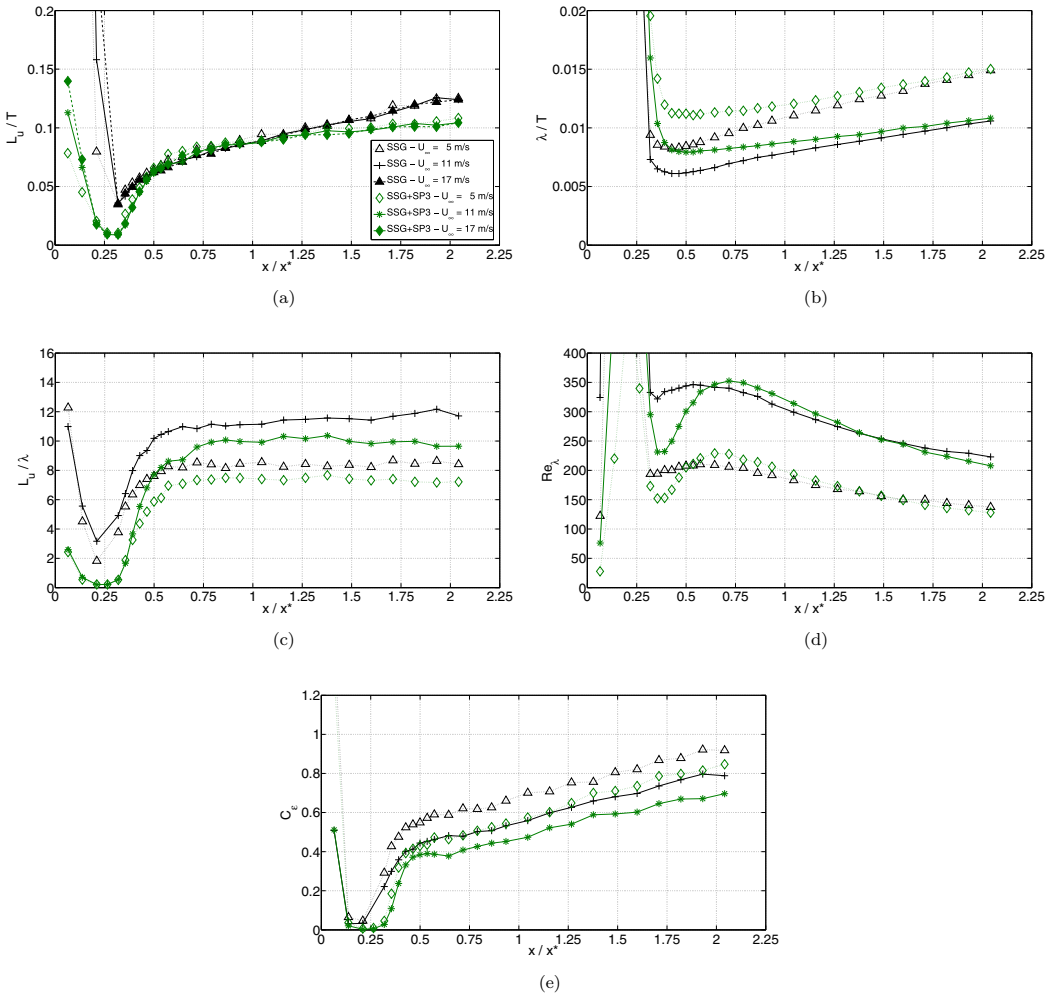

FIG. 16. (a) Integral length scale, (b) Taylor length scale, (c) ratio between integral and Taylor length scales, (d) Reynolds number based on Taylor length scale, and (e) dissipation coefficient for SSG (black) and SSG+SP3 (green) along the centerline. Data for $U_\infty = 17$ m/s are not shown for quantities derived from ε as explained in Sec. II D.

SSG and of SSG+SP3, where Re_λ is decreasing. Mazellier and Vassilicos [16] found that, in the turbulence decay region of fractal square grids, the value of L_u/λ grows with the inlet Reynolds number Re_{t_0}. In our experiment we find that, when considering SSG and SSG+SP3 separately, L_u/λ increases with U_∞ and therefore with Re_{t_0}. This is a consequence of the fact that λ reduces for increasing U_∞ (L_u is not significantly dependent on U_∞). Nevertheless, it is interesting to notice that the values of L_u/λ are different between SSG and SSG+SP3 even though U_∞ and t_0 (and therefore Re_{t_0}) are the same. The presence of the splitter plates at the very beginning of the production region modifies the streamwise development of the wakes originating from the bars of SSG (as we have seen for example from the increase in x_{peak}) and it affects the evolution of the turbulence scales along the centerline. In our case SSG and SSG+SP3 can be considered as two different turbulence generators and in particular we find that, by adding the splitter plates, the ratio L_u/λ decreases.

We are interested in studying if and how the higher-order statistics of u are influenced by the vortex shedding suppression. We first plot the skewness S [Fig. 17(a)] and the flatness F [Fig. 17(c)]

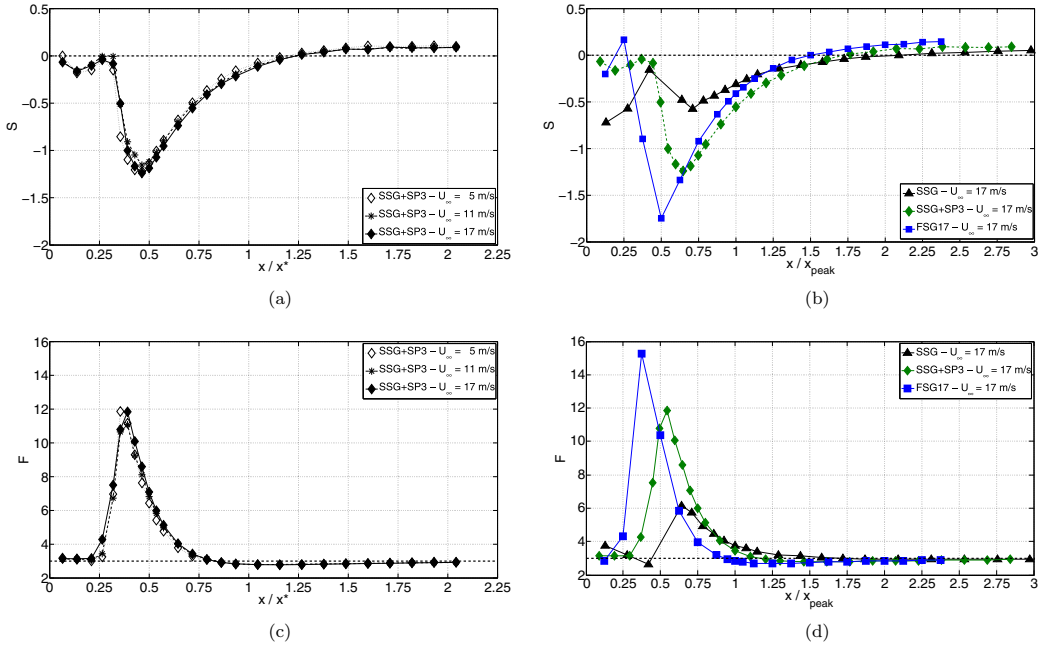

FIG. 17. (a) and (b) Skewness of u and (c) and (d) flatness of u for SSG+SP3 at $U_\infty = 5,11,17$ m/s (a) and (c) as a function of x/x^* and comparison with SSG and FSG17 for $U_\infty = 17$ m/s (b) and (d) as a function of x/x_{peak}. The horizontal dashed lines identify (a) and (b) $S = 0$ and (c) and (d) $F = 3$.

of u for SSG+SP3 at different values of U_∞. There is a good collapse between the results for the three inlet velocities. This ensures that S and F have no Reynolds dependence, at least in the range here investigated. The skewness is initially negative in the turbulence production region, reaching a minimum value around $x/x^* = 0.45$, before increasing further downstream and becoming positive in the far decay region, where it assumes small yet nonzero values, this being a typical feature of decaying grid-generated turbulence [37]. The flatness steeply increases in the production region, where it exhibits a peak around $x/x^* = 0.4$, and subsequently decreases towards values close to 3 in the decay region ($x/x^* > 0.8$).

At this point we compare the evolutions of S and F along the centerline for both SSG and SSG+SP3. The streamwise positions where the skewness [Fig. 17(b)] is minimum and the flatness [Fig. 17(d)] is maximum are very similar between SSG and SSG+SP3 in terms of x/x_{peak}. The most striking differences between the two configurations is that for SSG+SP3 (i) the skewness reaches more negative values in the production region and (ii) the flatness is higher. We also consider the results for FSG17, for which E_{sh} is the lowest, and we plot S and F for this grid in the same figures. We find that the absolute values of the skewness and the flatness reach the highest values for FSG17. Our results would suggest that an effect of vortex shedding in grid-generated turbulence is to "hide" the non-Gaussian behavior of u in the production region. In fact, when vortex shedding is highly energetic, S and F get closer to values typical of a Gaussian distribution, i.e., $S \to 0$ and $F \to 3$, in the production region too. In Appendix B we perform a simple exercise to show that an increase in the vortex shedding energy is consistent with a decrease in the absolute value of the skewness of u.

Wavelet transform in production and decay regions

In order to support our last observations on the Gaussianity of u, we look directly at the effects of vortex shedding on the statistics associated with the frequencies in the proximity of f_{sh}. For this purpose we perform a continuous wavelet transform of velocity signals obtained for all our four

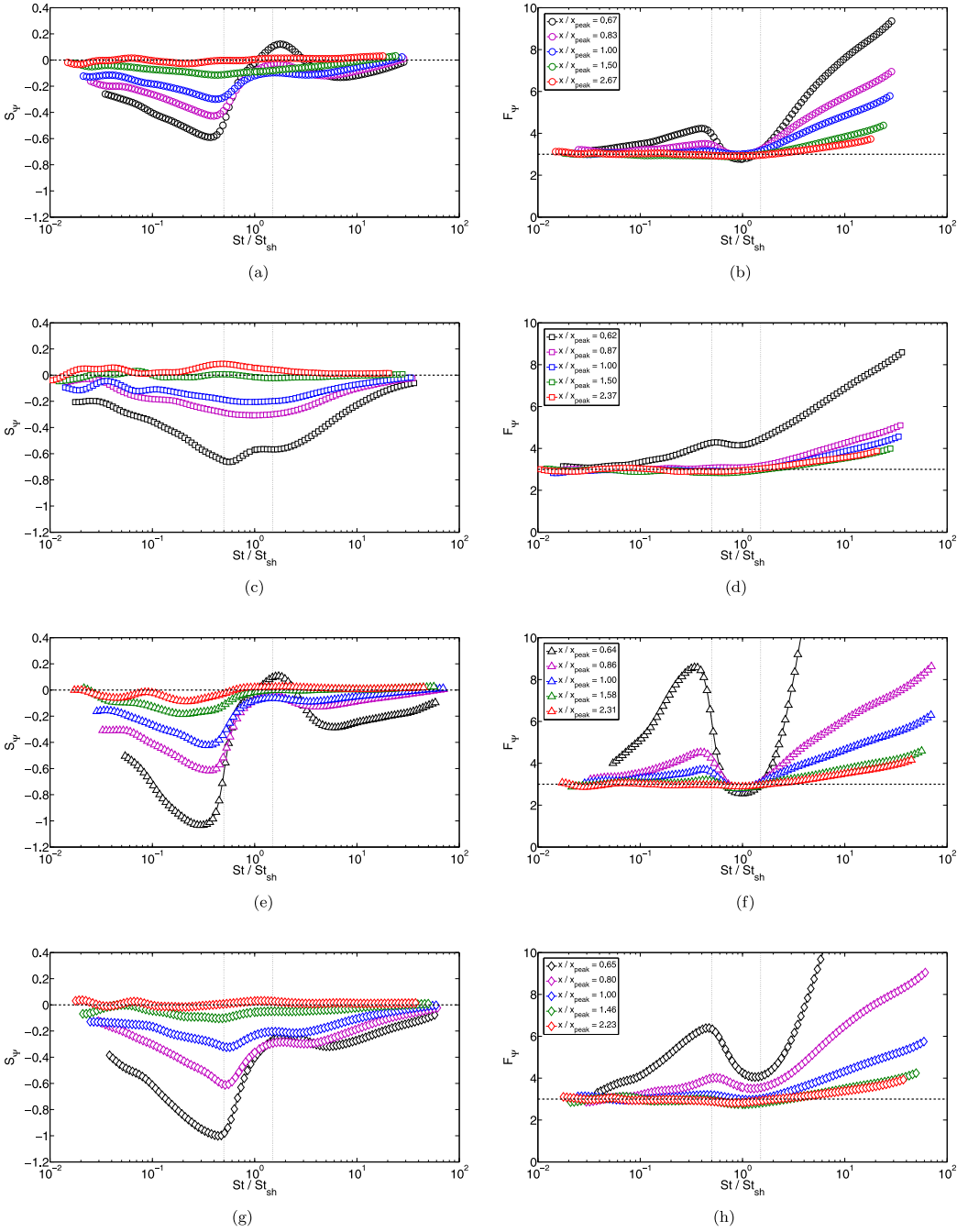

FIG. 18. Skewness (left column) and flatness (right column) of the wavelet transforms of u for (a) and (b) RG60, (c) and (d) FSG17, (e) and (f) SSG, and (g) and (h) SSG+SP3. The vertical dotted lines identify the interval $\Delta\mathrm{St}/\mathrm{St}_{sh} = 1$ centered across St_{sh}. The horizontal dashed lines identify $S_\Psi = 0$ (left column) and $F_\Psi = 3$ (right column); $U_\infty = 17$ m/s.

turbulence generators. This type of transform allows us to analyze the relative contributions of the scales a (time scales of dilatation) to the signal $u(t)$ at instants t'. The wavelet transform $u_\Psi(a,t')$ of

$u(t)$ is defined as [38]

$$u_\Psi(a,t') = a^{-1/2} \int u(t)\Psi^*\left(\frac{t-t'}{a}\right)dt, \tag{6}$$

where Ψ is the "mother" wavelet function (Ψ^* is its complex conjugate). The time scales a can be converted to (pseudo)frequencies f by taking into account the center frequency f_c at which the magnitude of the Fourier transform of Ψ is maximum. In our context we basically use this type of transform as a systematic way to apply a bandpass filter to the time series. The function Ψ can be indeed interpreted as a bandpass filter [39] whose amplitude depends on the particular choice of Ψ. In this analysis Ψ is chosen to be the Mexican hat function (second derivative of the Gaussian), as done, for example, in Ref. [40] and in Ref. [41]. From on operative point of view, the transforms $u_\Psi(a,t')$ are obtained by making use of the convolution theorem, i.e., the convolution in Eq. (6) is computed as the inverse Fourier transform of the product of the Fourier transforms of u and Ψ^*. Next, for every considered value of a, we compute the time statistics (third and fourth moments) of the wavelet coefficients.

We consider RG60, FSG17, SSG, and SSG+SP3 and, for each grid, we select five streamwise positions on the centerline, both in the production region and in the decay region. The locations are chosen in order to make a comparison at similar values of x/x_{peak} between the different configurations. For each time series, we limit the wavelet transform analysis to a range of frequencies $\Delta f_\Psi = [f_{\min}, f_{\max}]$. The value of $f_{\min}$ is chosen to be $50\,f_\Theta$, where f_Θ is the frequency associated with the integral time scale, and $f_{\max} = 0.1\,f_\eta$. The interval Δf_Ψ is discretized using 100 logarithmically spaced points.

We examine the skewness (Fig. 18, left column) $S_\Psi = \langle u_\Psi^3\rangle/\langle u_\Psi^2\rangle^{3/2}$ and the flatness (Fig. 18, right column) $F_\Psi = \langle u_\Psi^4\rangle/\langle u_\Psi^2\rangle^2$ of u_Ψ as a function of St/St_{sh} for the different configurations. We first look at the results for FSG17, since this is the grid where the vortex shedding is the least energetic and persistent. In the production region, S_Ψ is negative in a substantial range of St, exhibits a minimum value, and is instead near zero for very small and very large frequencies. When one moves to the decay region, the values of S_Ψ become closer to zero or weakly positive, consistent with the trend previously observed for the skewness of u [Fig. 17(b)]. The FSG17 differs from all the other configurations. In fact, in the production region of RG60, SSG, and SSG+SP3 the values of S_Ψ undergo a sudden increase towards zero in the proximity of $\text{St} = \text{St}_{sh}$. Analogously, for $\text{St} \approx \text{St}_{sh}$, the values of F_Ψ rapidly decrease approaching 3 in the production region, where vortex shedding is strong. On the contrary, when the vortex shedding is weaker, F_Ψ generally monotonically increases with increasing frequencies (the small scales are more intermittent), as is always the case for FSG17 (with the exception of the measurements at $x/x_{\text{peak}} = 0.62$).

Due to this analysis, we support and confirm the scenario suggested in Sec. IV B. In the production region of grid-generated turbulence, there is a correlation between the energy associated with the vortex shedding and the values of the skewness and the flatness of the velocity fluctuations. In particular, the skewness and the flatness approach values typical of a Gaussian distribution for an increasing vortex shedding energy contribution. When the vortex shedding is less important, the non-Gaussian behavior of the velocity fluctuations in the production region is more evident, i.e., the skewness is significantly negative and the flatness is much higher than 3.

V. CONCLUSION

In this paper we have characterized the flow downstream of different turbulence-generating grids in a wind tunnel, with hot-wire measurements performed mainly on the centerline. In particular, we have considered three types of grids: a regular grid (RG60), a fractal-square grid (FSG17), and a single-square grid (SSG) with the highest value of t_0/L_0.

For FSG17 and SSG, the maximum distance from the grids that we reach is not large enough to capture the classical $C_\varepsilon = \text{const}$. In fact, for both grids the ratio L_u/λ remains approximately

constant in the turbulence decay region, implying $C_\epsilon \propto \mathrm{Re}_\lambda^{-1}$ for a fixed inlet Reynolds number Re_{t_0}. For RG60, where the wake-interaction length scale x^* is the lowest, we do recover the $C_\varepsilon = \text{const}$ region of turbulence at $x/x_{\text{peak}} \gtrsim 5.5$.

The Strouhal number St_{sh} based on t_0, associated with the vortex shedding from the largest bars of the grids, is the highest for SSG ($\mathrm{St}_{sh} \approx 0.19$) and the lowest for FSG17 ($\mathrm{St}_{sh} \approx 0.13$). However, when the square root of the area of the bars ($\sqrt{t_0 L_0}$) is used for the definition of a Strouhal number St_{sh}^A, the values turn out to be approximately the same for both grids, $\mathrm{St}_{sh}^A \approx 0.43$ for SSG and $\mathrm{St}_{sh}^A \approx 0.44$ for FSG17.

In the production region and close to x_{peak}, the values of turbulence intensity Tu are higher for SSG than for FSG17, despite the former having the smallest blockage ratio σ and producing the lowest static pressure drop $C_{\Delta p}$. This result is achieved by making use of the scaling introduced in Ref. [17], i.e., increasing the ratio t_0/L_0 for SSG compared to FSG17. However, in the turbulence decay region, the values of Tu for SSG and FSG17 tend to collapse and they are considerably greater than for RG60, which has the highest σ and therefore produces the biggest $C_{\Delta p}$.

In the production region of SSG and even well beyond x_{peak}, a significant contribution to the turbulent kinetic energy u'^2 comes from the energy associated with a narrow range of St in the proximity of St_{sh}. This demonstrates that the higher values of Tu for SSG are mainly due to vortex shedding effects. We have investigated a three-dimensional turbulence generator (SSG+SP) designed for the study of vortex shedding suppression. We placed a set of four splitter plates in the production region of SSG. Hot-wire measurements were performed along the centerline for six distances x_{sp} of the splitter plates from the grid. Among the limited number of positions x_{sp}/t_0 tested here, the distance $x_{sp}/t_0 = 3$ is found to be the most effective in attenuating the vortex shedding in the present configuration. This value is close to $x_{sp}/D = 2.7$, which has been demonstrated to maximize vortex shedding suppression for a single circular cylinder with diameter D. For $x_{sp}/t_0 = 3$ the profiles of Tu show that (i) the distance x_{peak} is maximized and (ii) the value of $\mathrm{Tu}_{\text{peak}}$ is minimized. We deduce that, by attenuating the vortex shedding mechanism, the drag coefficient of the bars c_d is reduced, the wakes become narrower, and therefore they meet further downstream.

Focusing on the configuration with $x_{sp}/t_0 = 3$ (SSG+SP3), we estimated the energy E_{sh} associated with vortex shedding. In the production region and in the proximity of x_{peak}, E_{sh} is reduced for SSG+SP3 with respect to SSG, not only in absolute value but also as a share of u'^2. For the same $\Delta\,\mathrm{St}/\mathrm{St}_{sh}$, the ratio E_{sh}/u'^2 is even lower for the grid FSG17. For FSG17 the vortex shedding effects are less intense and less persistent on the centerline when compared, for the same x/x_{peak}, to all the other tested grids, both with a higher t_0 (SSG) and with a lower t_0 (RG60). Hence, similarly to fractal plates [7] and fractal trailing edges [19], fractal grids exhibit a weaker vortex shedding. This property could be due to the presence of the smaller geometrical iterations in the fractal geometries. However, while for fractal grids the shedding is less persistent downstream, for fractal plates the shedding is more persistent downstream (see [7]). More research is needed to explain this difference, but for FSG17, the interaction of different wakes with different sizes, which is absent for the other grids investigated here, is suggested to be the cause of the less intense and less persistent vortex shedding along the centerline.

When vortex shedding is suppressed, the growth of the integral length scale L_u becomes slower along the centerline. This feature is indeed observed for both SSG+SP3 and FSG17. In addition to this, in the turbulence decay region the ratio L_u/λ remains constant even when the splitter plates are added, but it is reduced for SSG+SP3 with respect to SSG, despite Re_{t_0} being the same.

We have considered the probability density functions of u, both in the production and in the decay regions, with particular focus on the evolution of the skewness S and the flatness F of u along the centerline. In the production region the values of S are negative and F is much higher than 3, in contrast to the decay region where the PDFs are close to a Gaussian distribution. Rare decelerating flow events are therefore more likely to occur than accelerating events in the turbulence production region. These features, previously observed for fractal square grids [16], seem to be intrinsic of the production region, as they are observable for all the turbulence generators here considered. However, for FSG17 these characteristics are more pronounced. We have found that

there is a correlation between the vortex shedding energy in the production region and the values of S and F. More specifically, when vortex shedding is less prominent, as is the case of FSG17, we find that $S \ll 0$ and $F \gg 3$. The non-Gaussian behavior of u in the production region is hidden when vortex shedding becomes important, i.e., $S \to 0$ and $F \to 3$ also in the production region in the presence of clear and intense vortex shedding. We checked the consistency of our observations by (i) comparing S and F for turbulence generators with different E_{sh}, (ii) carrying out an exercise (see Appendix B) where an artificial shedding contribution is added to a stochastic time series, and (iii) performing a continuous wavelet transformation of u for all the configurations, both in the production and in the decay region, and comparing the statistics of the wavelet transforms. Further research is still required in order to determine the origin of the strong decelerating events that occur in the turbulence production region. Here we have shown that they are not caused by the vortex shedding, which in fact masks them in the S and F statistics.

ACKNOWLEDGMENTS

The authors acknowledge support from the EU through the FP7 Marie Curie MULTISOLVE project (Grant Agreement No. 317269). J.C.V. also acknowledges the support of an ERC Advanced Grant (Project No. 320560). G.M. wishes to thank P. Baj for his useful comments during the postprocessing of the data.

APPENDIX A: GROWTH OF THE BOUNDARY LAYER ON THE WIND TUNNEL'S WALLS

In Sec. III A we have shown that for RG60 the mean velocity increases with x along the centerline for $x > 0.6$ m for both $U_\infty = 5$ and 17 m/s. In this Appendix we show that the increase of U that we have observed is consistent with the growth of a turbulent boundary layer on the wind tunnel's walls. If we consider the continuity equation it is easy to show that an increase in the boundary layer displacement thickness $\delta^*(x)$ leads to an increase in the mean velocity $U(x)$ according to

$$\delta^*(x) \propto \left(1 - \sqrt{\frac{U_\infty}{U(x)}}\right). \tag{A1}$$

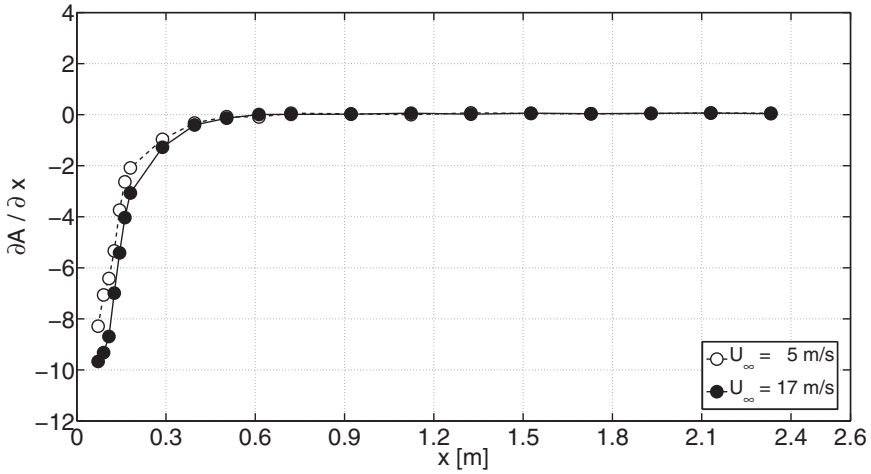

FIG. 19. Boundary layer growth for RG60.

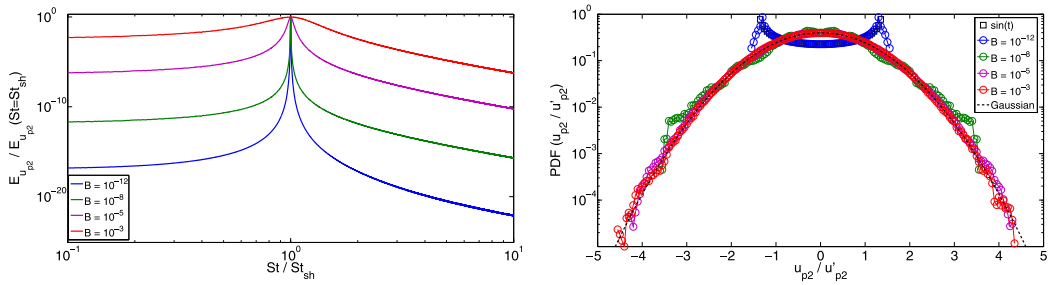

FIG. 20. (a) Power spectrum density and (b) PDF of u_{p2} for different values of the parameter B.

For a turbulent boundary layer the growth of the displacement thickness can be expressed as [42]

$$\frac{\delta^*(x)}{x} \propto \mathrm{Re}_x^{-1/7} \propto \left(\frac{U(x)x}{\nu}\right)^{-1/7}. \tag{A2}$$

From Eqs. (A1) and (A2) we obtain that if $U(x)$ increases as a result of the increase of $\delta^*(x)$ it must be verified that

$$\left(1-\sqrt{\frac{U_\infty}{U(x)}}\right)^{7/6}\left(\frac{U(x)}{\nu}\right)^{1/6} \propto x. \tag{A3}$$

Therefore, letting the left-hand side of Eq. (A3) be $A(x)$, it is sufficient to verify that $\partial A/\partial x$ is constant along x in the range where $U(x)$ is found to increase. Figure 19 shows that, for both $U_\infty = 5$ and 17 m/s, $\partial A/\partial x$ is constant along x for $x > 0.6$ m, which is exactly what we wanted to demonstrate.

APPENDIX B: EFFECT OF THE VORTEX SHEDDING ENERGY ON THE SKEWNESS

We consider a velocity signal resulting from the combination of a periodic component and a stochastic component. We carry out a simple exercise to show that, if the stochastic part is characterized by negative skewness, an increase in the energy associated to the periodic component is consistent with a decrease of the absolute value of the skewness of the total velocity signal.

We consider a stochastic signal $u_{tb2}(t)$, which is the fluctuating velocity time series relative to the hot-wire measurement performed for FSG17 at $x/x_{\mathrm{peak}} = 0.95$ for $U_\infty = 17$ m/s. At this location the frequency spectrum no longer shows a local peak at the vortex shedding Strouhal number $\mathrm{St}_{sh} = 0.126$. A periodic component $u_{p2}(t)$ is modeled with a sinusoidal series given by

$$u_{p2}(t) = \sum_i A_i \sin\left(2\pi \frac{St_i U_\infty}{t_0} t + \phi_i\right), \tag{B1}$$

TABLE III. Values of the skewness S of u_{tb}, u_p, and u_{tot} for different values of P and B.

	S			
u_{tb}		−0.49		
u_p		0.00		
u_{tot} $(P = 0.2)$	−0.35	−0.35	−0.35	−0.35
u_{tot} $(P = 0.4)$	−0.23	−0.22	−0.23	−0.22
u_{tot} $(P = 0.6)$	−0.12	−0.12	−0.13	−0.12
u_{tot} $(P = 0.8)$	−0.04	−0.04	−0.05	−0.04
	$(B = 10^{-12})$	$(B = 10^{-8})$	$(B = 10^{-5})$	$(B = 10^{-3})$

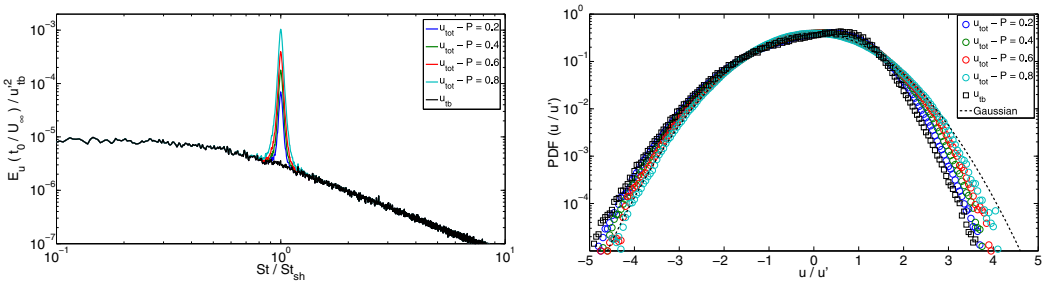

(a) (b)

FIG. 21. (a) Power spectrum density and (b) PDF of u_{tb} and $u_{\rm tot}$ for different values of P and $B = 10^{-5}$.

where each ϕ_i is a random variable with uniform distribution and taking values between $-\pi$ and π. The coefficients A_i are expressed as $A_i = [B + (\mathrm{St}_i - \mathrm{St}_{sh})^2]^{-1}$ in order to distribute most of the energy to the modes associated with St close to St_{sh}. Increasing the value of the parameter B has the effect of modeling a more broadband periodic component, as shown by the power spectrum density of u_{p2} [Fig. 20(a)] for different values of B. In Fig. 20(b) we show that with decreasing values of B (modeling a more narrow-band phenomenon) the PDF of u_{p2}/u'_{p2} tends to the distribution associated with $\sin(t)$, whereas with high values of B the PDF tends to a Gaussian distribution. We now consider a zero-mean signal $u_{\rm tot}(t)$ given by

$$u_{\rm tot}(t) = u_p(t) + u_{tb}(t), \tag{B2}$$

with

$$u_p(t) = \sqrt{P}\,\frac{u_{p2}(t)}{u'_{p2}}, \tag{B3}$$

$$u_{tb}(t) = \sqrt{1-P}\,\frac{u_{tb2}(t)}{u'_{tb2}}, \tag{B4}$$

where the parameter $P, 0 \leqslant P \leqslant 1$, is the fraction of the total kinetic energy assigned to the periodic component, $P = u'^2_p$. We always check *a posteriori* that $u'^2_{\rm tot} \approx 1$, thus verifying that $u_p(t)$ and $u_{tb}(t)$ are statistically independent.

At this point we set the parameter P to four different values, $P = 0.2, 0.4, 0.6, 0.8$, indicating the increasing importance of the periodic component in the total signal. We compute the skewness of $u_{\rm tot}(t)$ for the above-mentioned values of P and we do this for different choices of B. The results are reported in Table III and they indicate that the skewness decreases (in absolute value) and approaches zero as the percentage of the energy associated with the periodic component increases, irrespectively of the value of B. Figure 21(a) shows that the power spectrum density of $u_{\rm tot}$ is modified just in the proximity of $\mathrm{St} = \mathrm{St}_{sh}$ by the presence of a more intense periodic contribution, whereas in the remaining part there are no deviations from the case of u_{tb}. The effect of P on the PDFs of $u_{\rm tot}(t)/u'_{\rm tot}$, which become more and more symmetric as P increases, can be seen in Fig. 21(b), where they are compared to the distribution of $u_{tb}(t)/u'_{tb}$ (limit case for $P = 0$).

[1] D. Hurst and J. C. Vassilicos, Scalings and decay of fractal-generated turbulence, Phys. Fluids **19**, 035103 (2007).

[2] P. C. Valente and J. C. Vassilicos, The decay of turbulence generated by a class of multiscale grids, J. Fluid Mech. **687**, 300 (2011).

[3] K. Nagata, Y. Sakai, T. Inaba, H. Suzuki, O. Terashima, and H. Suzuki, Turbulence structure and turbulence kinetic energy transport in multiscale/fractal-generated turbulence, Phys. Fluids **25**, 065102 (2013).

[4] S. Weitemeyer, N. Reinke, J. Peinke, and M. Hölling, Multi-scale generation of turbulence with fractal grids and an active grid, Fluid Dyn. Res. **45**, 061407 (2013).
[5] K. H. H. Goh, P. Geipel, and R. P. Lindstedt, Lean premixed opposed jet flames in fractal grid generated multiscale turbulence, Combust. Flame **161**, 2419 (2014).
[6] R. Gomes-Fernandes, B. Ganapathisubramani, and J. C. Vassilicos, The energy cascade in near-field non-homogeneous non-isotropic turbulence, J. Fluid Mech. **771**, 676 (2015).
[7] J. Nedić, O. Supponen, B. Ganapathisubramani, and J. C. Vassilicos, Geometrical influence on vortex shedding in turbulent axisymmetric wakes, Phys. Fluids **27**, 035103 (2015).
[8] G. Cafiero, S. Discetti, and T. Astarita, Flow field topology of submerged jets with fractal generated turbulence, Phys. Fluids **27**, 115103 (2015).
[9] P. Baj, P. J. K. Bruce, and O. R. H. Buxton, The triple decomposition of a fluctuating velocity field in a multiscale flow, Phys. Fluids **27**, 075104 (2015).
[10] K. Nagata, H. Suzuki, Y. Sakai, T. Hayase, and T. Kubo, Direct numerical simulation of turbulent mixing in grid-generated turbulence, Phys. Scr. **T132**, 014054 (2008).
[11] S. Laizet and J. C. Vassilicos, Fractal space-scale unfolding mechanism for energy-efficient turbulent mixing, Phys. Rev. E **86**, 046302 (2012).
[12] H. Suzuki, K. Nagata, Y. Sakai, T. Hayase, Y. Hasegawa, and T. Ushijima, Direct numerical simulation of fractal-generated turbulence, Fluid Dyn. Res. **45**, 061409 (2013).
[13] Y. Zhou, K. Nagata, Y. Sakai, H. Suzuki, Y. Ito, O. Terashima, and T. Hayase, Relevance of turbulence behind the single square grid to turbulence generated by regular- and multiscale-grids, Phys. Fluids **26**, 075105 (2014).
[14] S. Laizet and J. C. Vassilicos, Stirring and scalar transfer by grid-generated turbulence in the presence of a mean scalar gradient, J. Fluid Mech. **764**, 52 (2015).
[15] T. Dairay, M. Obligado, and J. C. Vassilicos, Non-equilibrium scaling laws in axisymmetric turbulent wakes, J. Fluid Mech. **781**, 166 (2015).
[16] N. Mazellier and J. C. Vassilicos, Turbulence without Richardson-Kolmogorov cascade, Phys. Fluids **22**, 075101 (2010).
[17] R. Gomes-Fernandes, B. Ganapathisubramani, and J. C. Vassilicos, Particle image velocimetry study of fractal-generated turbulence, J. Fluid Mech. **711**, 306 (2012).
[18] S. Laizet, J. Nedić, and J. C. Vassilicos, The spatial origin of $-5/3$ spectra in grid-generated turbulence, Phys. Fluids **27**, 065115 (2015).
[19] J. Nedić and J. C. Vassilicos, Vortex shedding and aerodynamic performance of airfoil with multiscale trailing-edge modifications, AIAA J. **53**, 3240 (2015).
[20] H. Akilli, B. Sahin, and N. Filiz Tumen, Suppression of vortex shedding of circular cylinder in shallow water by a splitter plate, Flow Meas. Instrum. **16**, 211 (2005).
[21] A. Roshko, On the wake and drag of bluff bodies, J. Aeronaut. Sci. **22**, 124 (1955).
[22] C. J. Apelt and G. S. West, The effects of wake splitter plates on bluff-body flow in the range $10^4 < R < 5 \times 10^4$. Part 2, J. Fluid Mech. **71**, 145 (1975).
[23] M. S. M. Ali, J. Doolan, and V. Wheatley, Low Reynolds number flow over a square cylinder with a splitter plate, Phys. Fluids **23**, 033602 (2011).
[24] S. Y. Lin and T. M. Wu, Flow control simulations around a circular cylinder by a finite volume scheme, Numer. Heat Transfer Appl. A **26**, 301 (1994).
[25] J. Y. Hwang, K. S. Yang, and S. H. Sun, Reduction of flow-induced forces on a circular cylinder using a detached splitter plate, Phys. Fluids **15**, 2433 (2003).
[26] R. E. Seoud and J. C. Vassilicos, Dissipation and decay of fractal-generated turbulence, Phys. Fluids **19**, 105108 (2007).
[27] P. C. Valente and J. C. Vassilicos, The non-equilibrium region of grid-generated decaying turbulence, J. Fluid Mech. **744**, 5 (2014).
[28] S. R. Munshi, V. J. Modi, and T. Yokomizo, Fluid dynamics of flat plates and rectangular prisms in the presence of moving surface boundary-layer control, J. Wind Eng. Ind. Aerod. **79**, 37 (1999).
[29] S. B. Pope, *Turbulent Flows* (Cambridge University Press, Cambridge, 2000).
[30] S. Laizet and J. C. Vassilicos, DNS of fractal-generated turbulence, Flow Turbul. Combust. **87**, 673 (2011).

[31] J. I. Cardesa-Dueñas, T. B. Nickels, and J. R. Dawson, 2D PIV measurements in the near field of grid turbulence using stitched fields from multiple cameras, Exp. Fluids **52**, 1611 (2012).
[32] J. Nedić, B. Ganapathisubramani, and J. C. Vassilicos, Drag and near wake characteristics of flat plates normal to the flow with fractal edge geometries, Fluid Dyn. Res. **45**, 061406 (2013).
[33] R. Fail, J. A. Lawford, and R. C. W. Eyre, Low-speed experiments on the wake characteristics of flat plates normal to an airstream, Aeronautical Research Council Report No. 3120, 1959 (unpublished).
[34] E. A. Anderson and A. A. Szewczyk, Effects of a splitter plate on the near wake of a circular cylinder in 2 and 3-dimensional flow configurations, Exp. Fluids **23**, 161 (1997).
[35] Y. J. Chen and C. P. Shao, Suppression of vortex shedding from a rectangular cylinder at low Reynolds numbers, J. Fluids Struct. **43**, 15 (2013).
[36] J. C. Vassilicos, Dissipation in turbulent flows, Annu. Rev. Fluid Mech. **47**, 95 (2015).
[37] M. R. Maxey, The velocity skewness measured in grid turbulence, Phys. Fluids **30**, 935 (1987).
[38] M. Farge, Wavelet transforms and their application to turbulence, Annu. Rev. Fluid Mech. **24**, 395 (1992).
[39] S. G. Mallat, A theory for multiresolution signal decomposition: The wavelet representation, IEEE Trans. Pattern Anal. **11**, 674 (1989).
[40] F. Nicolleau and J. C. Vassilicos, Wavelets for the study of intermittency and its topology, Philos. Trans. R. Soc. London A **357**, 2439 (1999).
[41] S. G. Mallinson, J. A. Reizes, G. Hong, and P. S. Westbury, Analysis of hot-wire anemometry data obtained in a synthetic jet flow, Exp. Therm. Fluid Sci. **28**, 265 (2004).
[42] F. M. White, *Viscous Fluid Flow*, 3rd ed. (McGraw-Hill, New York, 2005).